ACS Catalysis

Article

Sulfated Tin Oxide as Highly Selective Catalyst for the Chlorination of Methane to Methyl Chloride

Youngmin Kim, Jip Kim, Hyun Woo Kim, Tae-Wan Kim, Hyung Ju Kim, Hyunju Chang, Min Bum Park, and Ho-Jeong Chae

ACS Catal., **Just Accepted Manuscript** • DOI: 10.1021/acscatal.9b02645 • Publication Date (Web): 06 Sep 2019

Just Accepted

is published by the American Chemical Society. 1155 Sixteenth Street N.W., Washington, DC 20036

Sulfated Tin Oxide as Highly Selective Catalyst for the Chlorination of Methane to Methyl Chloride

Youngmin Kim[†,1], Jip Kim[†,1,2], Hyun Woo Kim[3], Tae-Wan Kim[1,4], Hyung Ju Kim[1,4], Hyunju Chang[3], Min Bum Park[5], and Ho-Jeong Chae[,1,4]*

[1]Carbon Resources Institute, Korea Research Institute of Chemical Technology, Daejeon 34114, Republic of Korea

[2]Department of Chemical and Biomolecular Engineering, Sogang University, Seoul 04107, Republic of Korea

[3]Center for Molecular Modeling and Simulation, Korea Research Institute of Chemical Technology, Daejeon 34114, Republic of Korea

[4]Department of Green Chemistry & Biotechnology, University of Science and Technology, Daejeon 34113, Republic of Korea

[5]Department of Energy and Chemical Engineering, Incheon National University, Incheon 22012, Republic of Korea.

[†]These two authors contributed equally to this work.

ABSTRACT: The chlorination of methane (CH_4) is an attractive route to convert CH_4 into more valuable chemicals. The selective formation of methyl chloride (CH_3Cl) is a key process, but it is rather difficult to achieve with high selectivity due to a radical reaction. Catalytic ionic processes can be a solution. Herein, sulfated tin oxide (STO) was employed in the gas-phase catalytic chlorination of CH_4. The STO catalyst exhibited high selectivity to CH_3Cl (>96%) even at high CH_4 conversion. By applying a suite of physicochemical characterizations, it is shown that the strong Lewis acid sites on STO generated by the interaction of Sn and surface sulfate groups are mainly responsible for the highly selective CH_4 conversion. DFT calculations further revealed that STO surface can activate more Cl_2 molecules in a heterolytic manner, leading to better catalytic performances compared to SnO_2 and sulfated zirconia catalysts.

KEYWORDS: methane, chlorination, methyl chloride, sulfated tin oxide, heterogeneous catalysis, selectivity

1. INTRODUCTION

Methane (CH_4), the main component of natural gas, is an important feedstock for the synthesis of fuels and value-added chemicals, such as methanol, light olefins, and aromatics.[1-4] With ongoing discovery of large reserves of shale gas, the utilization of methane has received increased attention in recent years. At present, industrially, methane is converted into bulk chemicals via an indirect process. That is, methane is reformed to syngas ($CH_4 + H_2O \rightarrow CO + 3H_2$) first, and then the syngas is converted into higher hydrocarbons or oxygenates using the Fischer-Tropsch (FT) process.[5,6] The other routes includes sequential transformation of methane to syngas, syngas to methanol, and then methanol to olefins (MTO), methanol to gasoline (MTG), or methanol to aromatics (MTA).[7] However, these processes are complex, energy intensive, and the capital cost is high. Therefore, the direct conversion of methane to value-added products under mild conditions with much less energy has been a subject of great importance in economical methane utilization.

Many efforts have been given to the direct conversion of methane to the desirable products in high yields. Methane is an inert molecule that has perfectly symmetric structure. It is known that the activation of first C-H bond of methane is difficult because of very high dissociation energy (ca. 440 kJ mol^{-1}) and low polarity of C-H bond.[8] High temperature, pressure, and/or oxidizing agents are needed for the direct activation of methane, and at such conditions gas phase free-radical reactions dominantly occur, which results in lack of selectivity.[9] For the selective conversion of methane, catalysis will have to play a key role. Several different approaches for the direct conversion pathway of methane to chemicals have been proposed like thermal or catalytic pyrolysis[10], oxidative or nonoxidative coupling[5,11], partial oxidation[12], plasma process[13], halogenation[14], photo-catalysis[15,16], and membranes[17] etc. Among them CH_4 halogenation is one

of the more efficient process for the direct transformation of CH_4. This reaction can produce mono-methyl halides (CH_3X, where X is halogen), which can act as reaction intermediates like methanol (CH_3OH) to further produce higher hydrocarbons or oxygenates.[3,12,18] Since the reaction of methane with fluorine is too reactive to control the reaction (highly exothermic) and the reaction with iodine is too stable to proceed the reaction (endothermic), most of the research on the methane halogenation have focused on the use of chlorine or bromine as a halogen source.

Among the halogens, chlorine (Cl_2) is the most widely used element in worldwide industry, being largely applied as a building block in the manufacture of a variety of polymers (polyvinyl chloride (PVC), polyurethane (PU), and polycarbonate (PC)), drugs, and agricultural chemicals [19]. The use of chlorine in methane halogenation is beneficial for large-scale applications because of its proper reactivity, high availability, and low price.[20] Also, excess chlorine, which is harmful to the environment and human health, can also be effectively consumed via the CH_4 chlorination process. In this process, CH_4 reacts with Cl_2 to produce chlorinated mixtures of methyl chloride (CH_3Cl), methylene chloride (CH_2Cl_2), chloroform ($CHCl_3$), and carbon tetrachloride (CCl_4) with equimolar hydrogen chloride (HCl) (Eqs. 1-4).[21]

$$CH_4 + Cl_2 \rightarrow CH_3Cl + HCl \quad (1)$$

$$CH_4 + 2Cl_2 \rightarrow CH_2Cl_2 + 2HCl \quad (2)$$

$$CH_4 + 3Cl_2 \rightarrow CHCl_3 + 3HCl \quad (3)$$

$$CH_4 + 4Cl_2 \rightarrow CCl_4 + 4HCl \quad (4)$$

Industrially, CH_3Cl is an important product as a valuable starting material in the production of higher chlorinated products, silicones, and methyl cellulose.[22] It also can be potentially used for the production of olefins, gasoline, or aromatics.[23] While, CH_2Cl_2, $CHCl_3$, and CCl_4 are un-

desired products due to their harmful effects contributing to global warming, the depletion of the ozon layer, and the formation of photochemical smog.[24,25] Hence, CH_3Cl is the most desired product of the methane chlorination reaction. However, gas-phase CH_4 chlorination follows a free-radical chain mechanism yielding low selectivity toward the desired CH_3Cl, especially at high CH_4 conversion.[8,14]

Heterogeneous catalysts can facilitate the selective mono-chlorination of methane to produce methyl chloride under the proper reaction conditions. A few studies have been devoted to methane chlorination using heterogeneous catalysts. Heterogeneous catalytic gas-phase CH_4 chlorination was first reported in the mid 1980's by Olah et al.[26] They demonstrated that CH_4 could be selectively chlorinated to CH_3Cl over supported metal oxyhalides and Pt (or Pd) catalysts at relatively low temperature, but also at very low space velocity. They proposed that the process involves an ionic mechanism through electrophilic insertion reactions. Cl_2 is polarized at the Lewis acid sites of the catalyst and the Cl_2 species complexed to the catalyst surface activate the C-H bonds of CH_4 via formation of intermediate five-coordinated carbonium ions, and then subsequent halogenolysis to CH_3Cl. Complexing ability of the catalyst with chlorine and polarizability of chlorine on the catalyst surface are key factors in this mechanism. Later, several zeolites such as H-ZSM-5, H-mordenite, NaL, X, and Y were examined as acid catalysts for CH_4 chlorination, and the results showed that zeolites having higher acidity led to better selectivity toward CH_3Cl.[27] The zeolite catalysts, however, were rapidly deactivated in a short time due to the dealumination of the zeolite matrix by HCl. Sulfated zirconia (SZ), one of the strongest solid super acids, was also studied as a CH_4 chlorination catalyst to produce CH_3Cl with >90% selectivity, albeit at a CH_4 conversion of less than 10%.[28] It was observed that the selectivity decreased to ~70% when the methane conversion increased up to 24% over the SZ

catalyst. Very recently, Na et al. has investigated the simultaneous increase in CH_4 conversion and CH_3Cl selectivity using a Pt loaded NaY zeolite catalyst with a Frustrated Lewis Pairs system, but it still yielded a low CH_3Cl selectivity of ~60% at CH_4 conversion of ~35%.[29]

Sulfated tin oxide (STO) is known to possess strong acidic properties and belongs to the class of solid super acids. In previous reports, it was proved that the acid strength of STO is even higher than that of SZ.[30-32] The generation of strong Lewis acid sites by sulfate species is due to the presence of a covalent S=O bond, which acts as electron-withdrawing species followed by the inductive effect, making the Lewis acid strength of Sn^{4+} stronger.[33] Although STO has been used as a catalyst in various acid catalyzed reactions such as etherification[31], esterification[33,34], Friedel–Crafts acylation[35], alkylation[36], transesterification[37,38], dehydration[39], and epoxidation reactions[40], there has been no literature concerning the use of STO as a catalyst for CH_4 chlorination. Thus, in this work, STO was synthesized and investigated as a solid super acid catalyst in gas-phase CH_4 chlorination for the selective production of CH_3Cl. Un-sulfated pure tin oxide (SnO_2) and SZ catalysts were also prepared and tested for comparison. The STO catalyst could activate Cl_2 and sequentially CH_4 to produce CH_3Cl with consistently high selectivity even at high CH_4 conversion. The effects of sulfate amount, calcination temperature, methane to chlorine ratio, and gas hourly space velocity (GHSV) were also studied. The possible reason for the high selectivity to CH_3Cl over STO was discussed based on the calculations of density functional theory (DFT).

2. EXPERIMENTAL SECTION

2.1. Catalyst Synthesis. Under magnetic stirring, $SnCl_4 \cdot 5H_2O$ (100 g, 98%, Sigma-Aldrich) was dissolved in deionized water (2 L), and aqueous ammonia (28-30%, Sigma-Aldrich) was

dropwise added until the solution was adjusted to pH 8. The solution was continuously stirred overnight, and the precipitated product was washed with deionized water and collected by centrifugation. $Sn(OH)_4$ powder was obtained after drying at 100 °C for 12 h and grinding. The sulfation was performed by adding $Sn(OH)_4$ powder into the 3 M H_2SO_4 (95-98%, Sigma-Aldrich) aqueous solution (15 ml g^{-1}) and vortex mixed vigorously for 30 min. The sulfated hydroxide material was collected by centrifugation, dried at 100 °C for 12 h, and finally calcined at 500 °C (3.3 °C min^{-1}) in air for 3 h to form STO. For comparison, pure SnO_2 was prepared by the same procedure without the sulfating process. SZ was also prepared and tested as another reference catalyst. $Zr(OH)_4$ (97%, Sigma-Aldrich) was used as a precursor, and it was sulfated with 3 M H_2SO_4 aqueous solution and calcined at 500 °C (3.3 °C min^{-1}) in air for 3 h before use. In order to investigate the effect of catalyst preparation conditions on the methane chlorination reaction, we also prepared some more STO catalysts: i) sulfated with different concentrations of H_2SO_4 aqueous solution and calcined at the same 500 °C; ii) sulfated with the same 3 M H_2SO_4 but calcined at different temperatures. The catalysts were designated STO-xM H_2SO_4 (x = 1, 2, or 3) and STO-y °C (y = 400, 500, or 600), respectively. The other conditions were identical to those given above.

2.2. Catalyst Characterization. The crystallographic structures of the catalysts were confirmed by X-ray diffraction (XRD) (Rigaku Ultima IV) operating at 40 kV and 40 mA with a Ni-filtered Cu Kα (λ = 1.5418 Å) source. Fourier-transform infrared (FT-IR) spectra in the 400-4000 cm^{-1} wavenumber range were recorded on a Bruker ALPHA-T FT-IR spectrometer. The specific surface areas and pore sizes were calculated by the Brunauer-Emmett-Teller (BET) and Barrett-Joyner-Halenda (BJH) methods, respectively, by using N_2 adsorption-desorption at 77 K with a Micrometrics ASAP 2020 analyzer. The crystal morphologies were examined via

transmission electron microscope (TEM) (Tecnai G2 F30 S-Twin) operated at 300 kV. During the TEM measurement, elemental analysis was also carried out using an attached energy dispersive X-ray (EDX) spectrometer. The acid properties of the catalyst were studied by using temperature-programmed desorption of ammonia (NH_3-TPD) using a BELCAT-B analyzer equipped with a thermal conductivity detector (TCD). Temperature-programmed reduction (TPR) with CH_4 was also carried out on a same analyzer. The relative densities of Brønsted and Lewis acid sites were estimated using the pyridine FT-IR (Nicolet 6700) technique with self-supporting catalyst wafers. X-ray absorption near edge structure (XANES) and extended X-ray absorption fine structure (EXAFS) spectra were collected on the 7D beamline at Pohang Acceleration Laboratory (PLS-II, 3.0 GeV, Korea). Thermogravimetric analyses (TGA) were performed on a Thermo plus EVO II TG8120 series, where the weight losses were related to the combustion of coke contents. Those were further confirmed by using a Thermo Scientific Flash 2000 CHNS elemental analyzer (EA).

2.3. Reaction testing. CH_4 chlorination as well as CH_3Cl chlorination was carried out in an Inconel fixed-bed reactor (inner diameter = 7 mm, length = 460 mm) under atmospheric pressure at 300 - 350 °C. 0.5 g of the catalyst was loaded inside the fixed-bed reactor. The gas flows of CH_4 (99.999%, Rigas Korea), CH_3Cl (99.5%, Rigas Korea), Cl_2 (99.999%, Rigas Korea), and He (99.9999%, Daesung Gas) were adjusted using mass flow controllers (Line-Tech for CH_4 and He, Brooks for CH_3Cl and Cl_2). The stainless steel gas lines of the setup were heated to 150 °C to prevent product condensation and corrosion. In order to prevent Cl_2 and CH_4 (or CH_3Cl) from reacting in advance in the reactor voids, a Cl_2 gas line was installed to inject Cl_2 gas directly above the catalyst bed. Prior to the reaction, the catalyst was pretreated at 400 °C for 1 h in a flow of He (10 mL min^{-1}). The reactor was then set at the reaction temperature and fed with CH_4

(or CH_3Cl), Cl_2, and He. In a typical reaction, CH_4 chlorination sequentially proceeded with an increasing mode for 2 h at each temperature (300, 325, and 350 °C), and thus the total reaction time was around 6 h. To investigate the stability of the catalyst, the independent isothermal reactions were also performed at each temperature during about 6 h on stream. The products were analyzed online by a gas chromatography (GC) (Younglin GC-6100 series) equipped with a HP-PLOT Q column (30 m length, 0.53 mm diameter, 40 μm thickness) and a flammable ionization detector. After analysis, the gas exhausts were passed through a NaOH scrubber to remove HCl and unreacted Cl_2. The CH_4 conversion and product selectivity were calculated on a carbon mole basis and defined using the following equations.

Conversion (%) = [{carbon (mole) in initial CH_4 (or CH_3Cl) – carbon (mole) in CH_4 (or CH_3Cl) after reaction} / {carbon (mole) in initial CH_4 (or CH_3Cl)}] × 100

Selectivity (%) = [{carbon (mol) in a product} / {carbon (mol) in all product}] × 100

In the all reactions, the product mixture contained only CH_3Cl, CH_2Cl_2, $CHCl_3$, and unreacted CH_4, and no other organic species were detected (Supporting Information Figure S1). In addition, no evidence of coke content of the spent catalysts was confirmed by TGA (Figure S2) and EA (Table S1) analyses. Therefore, we simply calculated the carbon balance from the sum of CH_4, CH_3Cl, CH_2Cl_2, and $CHCl_3$, and the resulting carbon balance was confirmed to be ca. 100% under all the reaction conditions studied here (Table S2).

2.4. Computational Details. All DFT calculations were performed as implemented in the Vienna *ab initio* simulation package (VASP).[41,42] We employed the optB86b-vdW functional[43,44] to account for van der Waals interactions between molecules and catalytic surfaces. The pseudopotentials of all atoms were described using the projector augmented wave (PAW)

method. We sampled the Brillouin zone with 3×3×1 Monkhorst-pack *k*-point grids. The kinetic energy cutoff was set to 450 and 520 eV for structures containing Sn and Zr, respectively. The ZrO_2 (110) and SnO_2 (110) surfaces were modeled as 4×4 supercells using the bulk structure deposited at the Materials project[45] as explained in a previous report.[46] A total of four layers were included in our model and two upper layers were allowed to relax, while the two other layers were fixed during all calculations. Sulfated structures were generated by adding SO_4 moiety to two metal atoms exposed to the surface. Periodic boundary conditions were applied to all surface structures which were separated along the *c*-axis by a vacuum distance of 20 Å. All geometries were optimized until the force was less than 0.01 eV/Å. We computed the adsorption energies of Cl_2 and CH_3Cl by referencing the gas phase energies of the surfaces and adsorbed molecules. In our sign convention, energetically favorable or exothermic adsorptions show negative adsorption energies. In explaining the catalytic activity toward the electrophilic chlorination, we performed DFT calculations on catalytic surfaces with and without Cl atoms. For comparing the relative stability of surfaces, we ignored the spin polarization. Atomic charges were determined based on the Bader charge analysis.[47,48] In the case of STO, the C-H bond activation was investigated in a cluster model containing 27 Sn atoms in which the dangling bonds are properly terminated by hydrogen atoms. As a H atom of CH_4 or CH_3Cl approaches to Cl atom during the chlorination, the activation energy for the C-H bond can be estimated by scanning the H-Cl distance up to 1.4 Å. To understand the polarization effect of the Cl atom, we computed the C-H activation energies for a small model system including a CH_4 molecule and a Cl atom by adding a fixed amount of charge to the Cl atom. These computational modelings on C-H activation processes were performed at M06/6-31G(d,p) and LANL2DZ (for Sn atoms) level of theory with Q-Chem software package.[49]

3. RESULTS AND DISCUSSION

3.1. Physicochemical Properties of Synthesized Catalysts. Figure 1a shows the powder XRD patterns of the three representative catalysts (i.e., SnO_2, STO, and SZ) prepared in this study. Both the SnO_2 and STO samples show obvious X-ray peaks at 2θ = 27, 34, 38, 52, and 65°, which are assigned to the tetragonal phase of the rutile SnO_2 structure with P42/mnm symmetry.[33] On the other hand, the X-ray peaks for STO become much broader and the intensity is significantly decreased compared to those of un-sulfated SnO_2. This indicates a reduction in crystal size after sulfation, which was also reported in the literature.[50] The XRD pattern of SZ also shows five obvious peaks assigned to the tetragonal phase of ZrO_2.[51] The crystallite sizes of the three catalysts estimated from the Scherrer equation and the (110) and (101) X-ray peaks of SnO_2 and ZrO_2 (Figure 1a), respectively, were 10.1, 1.8, and 7.1 nm. The BET surface areas of the sulfated samples (i.e., 138 and 126 m^2 g^{-1} for SZ and STO, respectively) were much higher than that of the un-sulfated SnO_2 (25 m^2 g^{-1}) (Table 1) known that the smaller the crystal size, the higher the surface area.

Figure 1b shows the FT-IR spectra of the SnO_2, STO, and SZ catalysts. For all three catalysts, the IR bands around 3400 and 1630 cm^{-1} are due to the presence of surface hydroxyl groups and adsorbed water molecules, respectively.[34] The characteristic peaks in the region of 610-500 cm^{-1} are associated with the bending vibration of the Sn-O-Sn or Zr-O-Zr bonds.[52] Characteristic sulfate bands are generally observed in the range of 1000-1200 cm^{-1}, assigned to inorganic chelating bidentate sulfate ions coordinated to the metal cation.[53] Both STO and SZ show several bands around that region, while they cannot be observed in pure SnO_2. This confirms the presence of sulfate groups (SO_4^{2-}) on the surface of STO and SZ. We also note here that the intensity of the IR bands for SO_4^{2-} was much higher for SZ than STO, indicating more sulfate

groups were adsorbed on the SZ surface. This is well correlated with the elemental analysis, i.e., 2.6 and 3.0 wt% of sulfur in STO and SZ, respectively (Table 1).

Figure 2 shows the TEM and high resolution (HR) TEM images of the SnO_2, STO, and SZ catalysts. All the samples seem to have an agglomeration of irregular particles with small voids. From their HRTEM images, the average crystal sizes of SnO_2, STO, and SZ were estimated to be ca. 11, 4, and 7 nm, respectively (Table 1), which is in good agreement with the XRD analysis. Clear lattice fringes were also observed in all the samples with *d*-spacings of 0.33 and 0.29 nm, which can be indexed to the (110) SnO_2 and (111) ZrO_2 crystal planes, respectively.[54,55] To investigate the distribution of elements included in the catalysts, scanning TEM-EDX mapping was also performed for STO and SZ catalysts (Figure 3). The sulfur species of the sulfate groups were homogeneously distributed over the entire metal oxide surfaces of both catalysts.

Figure 4a displays the NH_3-TPD profiles for the SnO_2, STO, and SZ catalysts. The strength and distribution of acid sites calculated from the NH_3 desorption peak area are also listed in Table 1. The peaks in the range below 200 °C, 200-400 °C, and above 400 °C are normally attributed to weak, medium, and strong acid sites, respectively.[56] Obviously, STO has the largest acid site density, while SnO_2 has almost no acid sites. This is in good agreement with the previous report.[57] SZ has a broad peak below 400 °C and a relatively sharp peak around 520 °C. For STO, there are two intense peaks observed around 180 and 530 °C, and the areas are much larger than those for SZ, indicating that it has many more acid sites both with weak and strong acid strength.

To distinguish the Brønsted and Lewis acid sites, FT-IR spectra of the three catalysts chemisorbed pyridine were also obtained (Figure 4b). The IR bands around 1540 and 1450 cm^{-1}

are due to the adsorbed pyridine on Brønsted and Lewis acid sites, respectively. In addition, another intense band which appeared around 1490 cm^{-1} corresponds to the combination of Lewis and Brønsted acid sites.[58] SnO_2 shows almost no pyridine adsorption IR bands, while the bands for both the Lewis and Brønsted acid sites were significantly increased by sulfation (i.e., IR spectrum of STO). This is well correlated with the results from NH_3-TPD. The relative area ratio of Brønsted and Lewis acid sites (B/L) was calculated to be 2.5 and 7.8 for STO and SZ, respectively (Table 1). This indicates that both catalysts have absolutely more Brønsted acid sites, but the STO contains relatively more Lewis acid sites in comparison to SZ. The presence of stronger Lewis acid sites in STO compared to SZ is also indicated by the band shift to a high energy wavenumber region (1454 vs 1446 cm^{-1}).[33,59] The STO catalysts prepared with different sulfate concentration (STO-2M vs STO-3M) and calcination temperature (STO-400 ^{o}C vs STO-500 ^{o}C) were also compared for the pyridine-IR spectroscopy (Figure S3). As can be easily expected, the amount of acid sites for STO-2M was lower than that of STO-3M despite the similar B/L ratio (2.5). However, when decreasing the calcination temperature, the strength of Lewis acid was weaker while the amount of Lewis acid sites increased.

Figure 5a shows Sn K-edge XANES spectra for the SnO_2 and STO catalysts. The absorption edge structure of STO is similar to that of SnO_2. However, there is a slight shift to a higher energy in the edge position for the STO (29204.6 vs 29201.6 eV), indicating the oxidation state is increased due to its higher Lewis acid site density.[60,61] Figure 5b shows Fourier transforms (FT) of k^3-weighted Sn K-edge EXAFS spectra of SnO_2 and STO catalysts. The spectra of the samples appear to be quite similar to each other. Peaks at 1-2 Å result from Sn-O neighbors whereas peaks at 2-4 Å result from Sn-Sn neighbors. The FT-EXAFS data of SnO_2 and STO were curve fitted to obtain the structural parameters including coordination number (CN),

interatomic distances (R), and Debye-Waller factors (σ^2). As listed in Table 2, in both samples, the interatomic distances of Sn-O and Sn-Sn scatterings appeared to be the same. Curve fitting of the FT-EXAFS revealed that the Sn-O shells were located at 2.05 Å and the two Sn-Sn shells were located at about 3.2 and 3.7 Å, confirming that both samples are rutile SnO_2 structures.[62] The main difference between the spectra of SnO_2 and STO is in the coordination numbers of Sn-Sn neighbor shells. The decreased coordination numbers of the Sn-Sn shells in STO compared to SnO_2 indicates a smaller crystallite size in STO than SnO_2, which is consistent with the results from the XRD and TEM analyses. The increased coordination number of the Sn-O interaction for STO was also observed. This increase in Lewis acid sites by sulfation should have an influence on CH_4 chlorination (see below).

3.2. Methane Chlorination Reaction. Figure 6 shows the temperature-dependent CH_4 conversion and product distribution with the blank and three representative catalysts. STO and SZ were the catalysts prepared by sulfation with 3 M H_2SO_4 and calcination at 500 ^oC. It is noted that even in the blank reactor (Figure 6a), CH_4 was consumed with 3.6% of conversion at 300 °C. The conversion almost linearly increased with increasing temperature, and reached 17.5% at 350 °C. This should be due to non-catalytic, thermal radical chlorination. In this condition, the selectivity of the main product CH_3Cl exhibited a gradual decrease, from 95.3% at 300 °C to 79.2% at 350 °C. The amount of CH_2Cl_2 was rather small with a selectivity ranging from 4.7 to 18.6% according to the temperature. The product $CHCl_3$ started to appear at temperature ≥325 °C and was less than 2.2% up to 350 °C. CCl_4 was not detected throughout the investigated temperature range. The results for SnO_2 (Figure 6b) were quite similar to those obtained from the blank test, indicating pure SnO_2 had negligible catalytic effect on CH_4 chlorination. This is not very surprising because this un-sulfated catalyst has a negligible acid site density. On the other

hand, over the STO catalyst (Figure 6c), which had the largest acid site density among the catalysts studied here, CH_3Cl as the target product was mainly produced with a very high selectivity of 96.6% even at 350 °C and 22.3% of CH_4 conversion. This is unusual because higher (or lower) CH_4 conversion generally correlates with lower (or higher) CH_3Cl selectivity. Furthermore, no $CHCl_3$ and CCl_4 were detected at all the temperatures studied here. The medium acid catalyst level of SZ (Figure 6d) exhibited results similar to reported data. In that study, when the CH_4 conversion increased from 10 to 24%, the selectivity to CH_3Cl decreased from 90 to 70%.[28] Compared to the STO catalyst, although SZ resulted in a somewhat higher conversion of 25.6%, it showed a much lower CH_3Cl selectivity of 71.8% at 350 °C, giving similar product distributions to those obtained radical processes. It means that free radical reactions are still dominant with SZ catalyst.[63] It should be noted that the CH_4 conversion was negligible below 300 °C in our reaction system. As can be seen in Figure S4, all the blank and the reactions with the STO and SZ catalysts showed only less than 1% methane conversion at the reaction temperature of 200 °C and 250 °C.

If the gas phase radical mechanism applied for STO catalysts, we would expect a product distribution like that of blank test. However, the conversion and selectivity patterns of the STO catalysts were noticeably different from the blank. This difference suggests that the STO catalysts may possess distinct catalytic mechanism from the blank. Unlike the radical process, in an ionic catalytic process, CH_3Cl adsorbed on the catalytic active site (i.e., Lewis acid site) could not be converted to CH_2Cl_2 and further chlorinated forms, because Cl^- anion can be more easily decomposed from CH_3Cl rather than H. To prove this hypothesis, we also performed CH_3Cl chlorination reaction. In this experiment, chlorination was carried out by injecting CH_3Cl instead of methane as a reaction feed. We chose 300 and 325 °C as the reaction temperature, where the

STO catalyst is relatively stable. The CH_3Cl:Cl_2 ratio was also adjusted to 1:2 for diluted conditions of CH_3Cl. Figure 7 displays the reaction results. In the blank reaction (Figure 7a) following the radical mechanism, the conversion of CH_3Cl was much higher than that of CH_4 as expected. That is, the CH_3Cl conversion was about 59.1% at 300 °C, and the selectivity of CH_2Cl_2 and $CHCl_3$ was 69.2% and 30.8%, respectively. At 325 °C, the CH_3Cl conversion reached 86.0% and the product contained up to CCl_4. In this case, the selectivities of CH_2Cl_2, $CHCl_3$ and CCl_4 were 43.6%, 51.7% and 4.7%, respectively. On the other hand, very interestingly, it was observed that the conversion of CH_3Cl was very low in the reaction using STO catalyst (Figure 7b). At 300 °C and 325 °C, the CH_3Cl conversion was only 3.7% and 7.4%, respectively, and the product was found to be CH_2Cl_2 only. Thus, chlorination of CH_3Cl is not preferred on STO catalysts, which may also be evidence of high CH_3Cl selectivity of STO in CH_4 chlorination.

We found that the major difference between STO and SZ is in their acidic properties: (1) much more acid sites of STO than SZ especially in strong acid sites from NH_3-TPD (Figure 4a), and (2) relatively more Lewis acid sites (lower B/L ratio) with stronger Lewis acidity (band shift to high energy wavenumber) in STO compared to SZ from pyridine-IR (Figure 4b). These results suggest that over the strong Lewis acid sites, the non-selective thermal radical chlorination of CH_4 can be suppressed to lead better selectivity of the target CH_3Cl.

The results of the time-on-stream (TOS) performances at 300, 325 and 350 °C are shown in Figure S5. The conversion and selectivities to the three chloromethane compounds were almost maintained with TOS at lower temperatures, 300 and 325 ^{o}C. There was only slight increase or decrease. However, at 350 ^{o}C, the selectivity to CH_3Cl decreased with TOS but the conversion and the selectivities to CH_2Cl_2 and $CHCl_3$ increased. This means the STO catalyst lost the

catalytic property due to some reasons, and thus the free radical reaction occurred. One possibility is the active site poisoning by coke deposition, but this can be excluded because there was no coke species in the spent catalyst as described above. Then, another possibility is the leaching of active site. To verify this phenomenon, we measured the CH_4-TPR for the three catalysts. As shown in Figure S6, unlike the other two catalysts, STO was reduced at higher than 350 ^{o}C, which may be due to the reduction of SnO_x to Sn. Then, Sn can leach out as a following equation, $Sn + 2Cl_2 \rightarrow SnCl_{4,\ gas}$ (b.p. ~ 114 °C).

The effects of calcination temperature and sulfate content of STO catalyst on the CH_4 chlorination performance were evaluated at reaction temperatures of 300, 325, and 350 °C. As shown in Figure 8a, STO sulfated with 3 M H_2SO_4 and calcined at 500 °C (STO-500 °C) exhibited the highest conversion with a high CH_3Cl selectivity in the range of 96-98%. However, calcination at 600 °C resulted in lower sulfur content than 500 °C (0.9 vs 2.6 wt%), and thus STO-600 °C led to both lower conversion and lower CH_3Cl selectivity. In addition, with the increase in sulfur content (2.3-2.6 wt%) produced by increasing H_2SO_4 concentration (1-3 M), CH_4 conversion gradually increased at all reaction temperatures studied here, while the CH_3Cl selectivity remained almost constant >95% even at 350 °C (Figure 8b). Figure 8c shows the effect of molar ratio of CH_4:Cl_2 on conversion and selectivity over STO catalyst. It is well known that CH_4 conversion increases and CH_3Cl selectivity decreases with an increase in the relative amount of Cl_2 in the reactant mixture.[26,27] Over the STO catalyst, when the CH_4:Cl_2 ratio was changed from 1.5:1 to 1:3, CH_4 conversion drastically increased and reached 36% at 350 °C. We should note here that although CH_3Cl selectivity also decreased, the rate of decrease was relatively slow and reached 87% at 350 °C.

We also investigated the effects of GHSV for the CH_4 chlorination. The results of the GHSV experiments on the STO catalyst were compared with the blank reaction, which is a thermal radical reaction. The catalyst amount was the same and the flow rate was changed. As shown in Figure S7, both the blank and STO catalyst showed that the CH_4 conversion gradually decreased due to the decrease in contact time (or residence time) with increasing GHSV. Meanwhile, CH_3Cl selectivity showed different trends in the two reactions. In the blank reaction, as expected, CH_3Cl selectivity gradually increased as GHSV increased. This shows a typical characteristic of the free radical reaction, where shorter reaction times result in less polychlorinated products. On the other hand, reactions with STO catalysts maintain very high levels of CH_3Cl selectivity over the investigated temperature range and are slightly affected by the GHSV changes. In particular, it was observed that the CH_3Cl selectivity decreased even more in the case of the relatively harsh conditions of the reaction temperature of 350 °C and the space velocity of 4000 ml h^{-1} g^{-1}. The decreased selectivity under higher GHSV could be due to the deactivation of the catalyst caused by contacting the catalyst with a relatively large amount of methane and chlorine per unit time, in which the reduction of the catalytic function, i.e., the loss of the active site by leaching, could be accelerated.

From the overall results, we demonstrated that although the free radical reaction cannot be completely ruled out, these experimental results suggest that the reaction on the surface of the STO catalyst works predominantly through a different reaction pathway than the radical mechanism.

3.3. DFT Calculations. To understand the outstanding performance of the STO catalyst in the methane chlorination, we computationally investigated the interactions between Cl atoms and the (110) surfaces of SnO_2, STO, and SZ with DFT calculations. By forming or breaking the Cl-Cl

bond, two atomistic models were prepared for each surfaces. Considering experimental evidences, we construct our computational models by assuming that Cl_2 molecules are cleaved heterolytically on surfated surfaces, i.e., the Cl_2 molecules are dissociated in two different species like $Cl^{\delta+}$ and $Cl^{\delta-}$, on STO and SZ surfaces while they are cleaved homolytically on SnO_2 surface. Although these models have fundamental limitations as we performed DFT calculations on representative structures, they are reasonable as the electrophilic halogenation is initiated by forming a complex of the super-acidic catalyst and a polarized halogen molecule.[28] In addition, we also checked the homolytic dissociation of Cl_2 molecules on STO surface and observed that heterolytic cleavage of Cl_2 molecule is favored for the STO catalyst. As shown in Figure 9, we found that the STO surface stabilizes dissociated Cl atoms more than SZ and SnO_2 surfaces. This computational result suggests that the STO surface can activate more Cl_2 molecules in a heterolytic manner compared to other surfaces, and positively charged Cl atoms on the STO surface can substitute a hydrogen atom in methane molecules through electrophilic insertion reaction.[18] On the other hand, these heterolytically dissociated $Cl^{\delta+}$ atoms on the STO have the positive charge of 0.32 as estimated from the Bader charge analysis,[47,48] which is lower than that (0.53) on the SZ surface. In addition, the activation energy of C-H bond in CH_4 is inversely proportional to the positive charges on Cl atoms (Figure S8). In other words, the C-H activation of CH_4 is more difficult on the STO surface. This result may be the reason why SZ catalyst showed the higher conversion than STO as discussed in Figure 6.

We also checked the adsorption energy of the Cl_2 molecule on these surfaces. Surface structures with adsorbed Cl_2 and CH_3Cl molecules are shown in the Figure 10. Cl_2 adsorption energies were negative for all the surfaces, indicating that those (110) surfaces were stabilized by an adsorbed Cl_2 molecule. The STO(110) surface showed the most negative adsorption energy of

-0.81 eV, while the SnO_2(110) surface showed the least negative value of -0.67 eV. A similar trend was also observed for the SZ (-0.77 eV) and ZrO_2 (-0.71 eV) (110) surfaces. This implies that both STO and SZ surfaces favor the adsorption of Cl_2 molecules possibly due to the partial positive charges on the surface developed by the electron-withdrawing sulfate group. For understanding the higher selectivity toward the mono-chlorination, we additionally prepared the surface structures with adsorbed CH_3Cl molecules. The adsorption energy of CH_3Cl on the STO(110) surface can also be calculated as the most negative (-1.20 eV) compared to those for SnO_2(110) and SZ(110) surfaces (-1.03 and -0.82 eV, respectively). In addition, we computationally estimated the transition state energy for activating a C-H bond in CH_4 and CH_3Cl (Figure S9). It was observed that CH_3Cl was detached from the catalyst surface in the transition state structure, which means that CH_3Cl on STO should overcome the high adsorption energy to proceed the reaction through the transition state structure. More importantly, in contrast to C-H activation by Cl radicals in the gas phase (Figures S9a and b), it has been found that C-H activation becomes more difficult after the mono-chlorination for STO (Figures S9c and d). Thus, it can be speculated that STO prevents the further chlorination of CH_3Cl by holding CH_3Cl molecules stronger than other catalysts, which also can be supported by the results of CH_3Cl chlorination experiments (Figure 7).

3.4. Relationship between Conversion and Selectivity. Figure 11 summarizes the relationship between CH_4 conversion and CH_3Cl selectivity over the several solid catalysts studied here, and reported in some literature.[64-72] It is obvious that there appears to be an inverse linear relationship between the CH_4 conversion and CH_3Cl selectivity. The SZ and its several derivative catalysts display enhanced selectivity to CH_3Cl compared to the trade-off line of blank run or SnO_2 at the same conversion level, but the differences are not very great. Most

interestingly, the STO catalysts exhibit remarkably enhanced CH_3Cl selectivity compared to the other catalytic results. At 25% CH_4 conversion, the selectivity was almost 90%, which is 25% higher than the trade-off line. Despite the large number of disparate approaches for direct CH_4 transformation, none of them has been developed into an industrial process. One of the biggest problems is the very low selectivity to desired product with reasonably high CH_4 conversion. For example, when considering the results of direct CH_4 to CH_3OH, which can act as a platform molecule like CH_3Cl, the most sophisticated homogeneous and heterogeneous catalysts showed below 90% selectivity to CH_3OH, with only 10% CH_4 conversion.[73] Therefore, the highly selective CH_4 chlorination over STO catalyst has the potential to advance the commercialization of the direct methane transformation process.

4. CONCLUSION

In this study, we have demonstrated that STO efficiently catalyzed the chlorination of CH_4 to CH_3Cl with good conversion and high selectivity compared to other catalyst systems. Based on the experimental and computational results, we speculate that the improved performance of STO is likely due to the abundant presence of strong Lewis acid sites developed by the interaction of Sn and surface sulfate groups, thus improving adsorption of Cl_2 and CH_3Cl on the catalyst surfaces. It was also computationally shown that heterolytic cleavage of Cl_2 molecule is more favored for the surface of STO and positively charged Cl atoms can activate C-H bond and promote the electrophilic chlorination. This work on the chlorination of CH_4 over STO suggests an interesting alternative for activating CH_4 to valuable chemicals. We will undertake more detailed mechanistic studies in the near future with advanced operando characterization and theoretical modeling to understand how the selective chlorination of CH_4 occurs on the surface of STO catalysts.

AUTHOR INFORMATION

Corresponding Author

* E-mail: hjchae@krict.re.kr (H.-J. Chae)

Author Contributions

The manuscript was written through contributions of all authors. All authors have given approval to the final version of the manuscript. †These authors contributed equally.

Notes

The authors declare no competing financial interest.

ASSOCIATED CONTENT

Supporting Information.

The Supporting Information is available free of charge on the ACS Publication website at DOI:. Elemental analysis of spent catalyst. Summary of catalyst performance. Gas chromatographs. TGA curves for the fresh and spent catalysts. FT-IR spectra of pyridine adsorption. CH_4 chlorination reaction results at low temperature. Time on stream in CH_4 chlorination. CH_4-TPR curves. GHSV effect in CH_4 chlorination. Effect of the positive charged Cl atom to the C-H activation energy. Transition state energies for the C-H activation of CH_4 and CH_3Cl.

ACKNOWLEDGMENT

This work was supported by the C1 Gas Refinery Program through a grant from the National Research Foundation of Korea (NRF) funded by the Ministry of Science and ICT (2016M3D3A1A01913251).

REFERENCES

1. Gesser, H. D.; Hunter, N. R. The Direct Conversion of Methane to Methanol by Controlled Oxidation. *Chem. Rev.* **1985**, *85*, 235–244.

2. Holmen, A. Direct Conversion of Methane to Fuels and Chemicals. *Catal. Today* **2009**, *142*, 2–8.

3. Tang, P.; Zhu, Q.; Wu, Z.; Ma, D. Methane Activation: the Past and Future. *Energy Environ. Sci.* **2014**, *7*, 2580–2591.

4. Sushkevich, V. L.; Palagin, D.; Ranocchiari, M.; van Bokhoven, J. A. Selective Anaerobic Oxidation of Methane Enables Direct Synthesis of Methanol. *Science* **2017**, *356*, 523–527.

5. Lunsford, J. H. Catalytic Conversion of Methane to More Useful Chemicals and Fuels: A Challenge for the 21st Century. *Catal. Today* **2000**, *63*, 165–174.

6. Karakaya, C.; Kee. R. J. Progress in the Direct Catalytic Conversion of Methane to Fuels and Chemicals. *Prog. Energy Combust. Sci.* **2016**, *55*, 60–97.

7. Schwach, P.; Pan, X.; Bao, X. Direct Conversion of Methane to Value-Added Chemicals over Heterogeneous Catalysts: Challenges and Prospects. *Chem. Rev.* **2017**, *117*, 8497−8520.

8. Horn, R.; Schlogl, R. Methane Activation by Heterogeneous Catalysis. *Catal. Lett.* **2015**, *145*, 23–39.

9. Havran, V.; Dudukovic, M. P.; Lo, C. S. Conversion of Methane and Carbon Dioxide to Higher Value Products. *Ind. Eng. Chem. Res.* **2011**, *50*, 7089–7100.

10. Xie, P.; Pu, T.; Nie, A.; Hwang, S.; Purdy, S. C.; Yu, W.; Su, D.; Miller, J. T.; Wang. C. Nanoceria-Supported Single-Atom Platinum Catalysts for Direct Methane Conversion. *ACS Catal.* **2018**, *8*, 4044−4048.

11. Xiao, Y.; Varma, A. Highly Selective Nonoxidative Coupling of Methane over Pt-Bi Bimetallic Catalysts. *ACS Catal.* **2018**, *8*, 2735−2740.

12. Alvarez-Galvan, M. C.; Mota, N.; Ojeda, M.; Rojas, S.; Navarro, R. M.; Fierro, J. L. G. Direct Methane Conversion Routes to Chemicals and Fuels. *Catal. Today* **2011**, *171*, 15–23.

13. Rutberg, P. G.; Kuznetsov, V. A.; Popov, V. E.; Popov, S. D.; Surov, A. V.; Subbotin, D. I.; Bratsev, A. N. Conversion of Methane by CO_2 + H_2O + CH_4 Plasma. *Appl. Energy* **2015**, *148*, 159–168.

14. Degirmenci, V.; Uner, D.; Yilmaz, A. Methane to Higher Hydrocarbons via Halogenation. *Catal. Today* **2005**, *106*, 252–255.

15. Yuliati, L.; Yoshida, H. Photocatalytic Conversion of Methane. *Chem. Soc. Rev.* **2008**, *37*, 1592–1602.

16. Chen, X.; Li, Y.; Pan, X.; Cortie, D.; Huang, X.; Yi, Z. Photocatalytic Oxidation of Methane over Silver Decorated Zinc Oxide Nanocatalysts. *Nat. Commun.* **2016**, *7*, 12273.

17. Morejudo, S. H.; Zanón, R.; Escolástico, S.; Yuste-Tirados, I.; Malerød-Fjeld, H.; Vestre, P. K.; Coors, W. G.; Martínez, A.; Norby, T.; Serra, J. M.; Kjølseth. C. Direct Conversion of Methane to Aromatics in a Catalytic Co-Ionic Membrane Reactor. *Science* **2016**, *353*, 563–566.

18. Olah, G. A. Electrophilic Methane Conversion. *Acc. Chem. Res.* **1987**, *20*, 422–428.

19. Lin, R.; Amrute, A. P.; Pérez-Ramírez, J. Halogen-Mediated Conversion of Hydrocarbons to Commodities. *Chem. Rev.* **2017**, *117*, 4182−4247.

20. Pérez-Ramírez, J.; Mondelli, C.; Schmidt, T.; Schluter, O. F.-K.; Wolf, A.; Mleczko, L.; Dreier, T. Sustainable Chlorine Recycling via Catalysed HCl Oxidation: From Fundamentals to Implementation. *Energy Environ. Sci.* **2011**, *4*, 4786–4799.

21. McBee, E. T.; Hass, H. B.; Neher, C. M.; Strickland, H. Chlorination of Methane. *Ind. Eng. Chem.* **1942**, *34*, 296–300.

22. McInroy, A. R.; Lundie, D. T.; Winfield, J. M.; Dudman, C. C.; Jones, P.; Lennon, D. Improved Atom Efficiency via an Appreciation of the Surface Activity of Alumina Catalysts: Methyl Chloride Synthesis. *Appl. Catal. B-Environ.* **2007**, *70*, 606–610.

23. Yingxu, W.; Dazhi, Z.; Zhongmin, L.; Bao-Lian, S. Methyl Halide to Olefins and Gasoline over Zeolites and SAPO Catalysts: A New Route of MTO and MTG. *Chin. J. Catal.* **2012**, *33*, 11–21.

24. Martin-Martinez, M.; Gómez-Sainero, L. M.; Alvarez-Montero, M. A.; Bedia, J.; Rodriguez, J. J. Comparison of Different Precious Metals in Activated Carbon-Supported Catalysts for the Gas-phase Hydrodechlorination of Chloromethanes. *Appl. Catal. B-Environ.* **2013**, *132–133*, 256–265.

25. Arevalo-Bastante, A.; Álvarez-Montero, M. A.; Bedia, J.; Gómez-Sainero, L. M.; Rodriguez, J. J. Gas-phase Hydrodechlorination of Mixtures of Chloromethanes with Activated Carbon-Supported Platinum Catalysts. *Appl. Catal. B-Environ.* **2015**, *179*, 551–557.

26. Olah, G. A.; Gupta, B.; Farina, M.; Felberg, J. D.; Ip, W. M.; Husain, A.; Karpeles, R.; Lammertsma, K.; Melhotra, A. K.; Trivedi, N. J. Selective Monohalogenation of Methane over Supported Acid or Platinum Metal Catalysts and Hydrolysis of Methyl Halides over y-Alumina-Supported Metal Oxide/Hydroxide Catalysts. A Feasible Path for the Oxidative Conversion of Methane into Methyl Alcohol/Dimethyl Ether. *J. Am. Chem. Soc.* **1985**, *107*, 7097–7105.

27. Bucsi, I.; Olah, G. A. Selective Monochlorination of Methane over Solid Acid and Zeolite Catalysts. *Catal. Lett.* **1992**, *16*, 27–38.

28. Batamack, P.; Bucsi, I.; Molnar, A.; Olah, G. A. Electrophilic Chlorination of Methane over Superacidic Sulfated Zirconia. *Catal. Lett.* **1994**, *25*, 11–19.

29. Joo, H.; Kim, D.; Lim, K. S.; Choi, Y. N.; Na, K. Selective Methane Chlorination to Methyl Chloride by Zeolite Y-based Catalysts. *Solid State Sci.* **2018**, *77*, 74–80.

30. Yu, H.; Fang, H.; Zhang, H.; Li, B.; Deng, F. Acidity of Sulfated Tin Oxide and Sulfated Zirconia: A View from Solid-State NMR Spectroscopy. *Catal. Commun.* **2009**, *10*, 920–924.

31. Furuta, S.; Matsuhashi, H.; Arata, K., Catalytic Action of Sulfated Tin Oxide for Etherification and Esterification in Comparison with Sulfated Zirconia. *Appl. Catal. A-Gen.* **2004**, *269*, 187–191.

32. Matsuhashi, H.; Miyazaki, H.; Kawamura, Y.; Nakamura, H.; Arata, K. Preparation of A Solid Superacid of Sulfated Tin Oxide with Acidity Higher than That of Sulfated Zirconia and Its Applications to Aldol Condensation and Benzoylation. *Chem. Mater.* **2001**, *13*, 3038–3042.

33. Khder, A. S.; El-Sharkawy, E. A.; El-Hakam, S. A.; Ahmed, A. I. Surface Characterization and Catalytic Activity of Sulfated Tin Oxide Catalyst. *Catal. Commun.* **2008**, *9*, 769–777.

34. Moreno, J. I.; Jaimes, R.; Gómez, R.; Nino-Gómez, M. E. Evaluation of Sulfated Tin Oxides in the Esterification Reaction of Free Fatty Acids. *Catal. Today* **2011**, *172*, 34–40.

35. Du, Y.; Liu, S.; Zhang, Y.; Yin, C.; Di, Y.; Xiao, F. -S. Mesostructured Sulfated Tin Oxide and Its High Catalytic Activity in Esterification and Friedel–Crafts Acylation. *Catal. Lett.* **2006**, *108*, 155–158.

36. Zhou, L.; Xu, B.; Hua, W.; Yue, Y.; Gao, Z. Sulfated Tin Oxide: An Efficient Catalyst for Alkylation of Hydroquinone with Tert-Butanol. *Catal. Commun.* **2008**, *9*, 2274–2277.

37. Lam, M. K.; Lee, K. T.; Mohamed, A. R. Sulfated Tin Oxide as Solid Superacid Catalyst for Transesterification of Waste Cooking Oil: An Optimization Study. *Appl. Catal. B-Environ.* **2009**, *93*, 134–139.

38. Lam, M. K.; Lee, K. T. Accelerating Transesterification Reaction with Biodiesel as Co-Solvent: A Case Study for Solid Acid Sulfated Tin Oxide Catalyst. *Fuel* **2010**, *89*, 3866–3870.

39. Dabbawala, A. A.; Mishra, D. K.; Hwang, J. -S. Sulfated Tin Oxide as An Efficient Solid Acid Catalyst for Liquid Phase Selective Dehydration of Sorbitol to Isosorbide. *Catal. Commun.* **2013**, *42*, 1–5.

40. Somidi, A. K. R.; Sharma, R. V.; Dalai, A. K. Synthesis of Epoxidized Canola Oil using A Sulfated-SnO_2 Catalyst. *Ind. Eng. Chem. Res.* **2014**, *53*, 18668−18677.

41. Kresse, G.; Furthmuller, J. Efficient Iterative Schemes for Ab Initio Total-Energy Calculations using A Plane-Wave Basis Set. *Phys. Rev. B* **1996**, *54*, 11169.

42. Kresse, G.; Joubert, D. From Ultrasoft Pseudopotentials to the Projector Augmented-Wave Method. *Phys. Rev. B* **1999**, *59*, 1758.

43. Klimes, J.; Bowler, D. R.; Michaelides, A. Chemical Accuracy for the Van der Waals Density Functional. *J. Phys.: Condens. Matter* **2010**, *22*, 022201.

44. Klimes, J.; Bowler, D. R.; Michaelides, A. Van der Waals Density Functionals Applied to Solids. *Phys. Rev. B* **2011**, *83*, 195131.

45. Jain, A.; Ong, S. P.; Hautier, G.; Chen, W.; Richards, W. D.; Dacek, S.; Cholia, S.; Gunter, D.; Skinner, D.; Ceder, G.; Persson, K. A. Commentary: the Materials Project: A Materials Genome Approach to Accelerating Materials Innovation. *APL Mater.* **2013**, *1*, 011002.

46. Tran, R.; Xu, Z.; Radhakrishnan, B.; Winston, D.; Sun, W.; Persson, K. A.; Ong, S. P. Surface Energies of Elemental Crystals. *Sci. Data* **2016**, *3*, 160080.

47. Bader, R. F. W. Atoms in Molecules. *Acc. Chem. Res.* **1985**, *18.1*, 9-15.

48. Tang, W.; Sanville, E.; Henkelman, G. A Grid-based Bader Analysis Algorithm without Lattice Bias. *J. Phys.: Condens. Matter* **2009**, *21*, 084204.

49. Shao, Y.; Gan, Z.; Epifanovsky, E.; Gilbert, A. T. B.; Wormit, M.; Kussmann, J.; Lange, A. W.; Behn, A.; Deng, J.; Feng, X.; Ghosh, D.; Goldey, M.; Horn, P. R.; Jacobson, L. D.; Kaliman, I.; Khaliullin, R. Z.; Kuś, T.; Landau, A.; Liu, J.; Proynov, E. I.; Rhee, Y. M.; Richard, R. M.; Rohrdanz, M. A.; Steele, R. P.; Sundstrom, E. J.; Woodcock, H. L.; Zimmerman, P. M.; Zuev, D.; Albrecht, B.; Alguire, E.; Austin, B.; Beran, G. J. O.; Bernard, Y. A.; Berquist, E.; Brandhorst,

K.; Bravaya, K. B.; Brown, S. T.; Casanova, D.; Chang, C.-M.; Chen, Y.; Chien, S. H.; Closser, K. D.; Crittenden, D. L.; Diedenhofen, M.; DiStasio, R. A.; Do, H.; Dutoi, A. D.; Edgar, R. G.; Fatehi, S.; Fusti-Molnar, L.; Ghysels, A.; Golubeva-Zadorozhnaya, A.; Gomes, J.; Hanson-Heine, M. W. D.; Harbach, P. H. P.; Hauser, A. W.; Hohenstein, E. G.; Holden, Z. C.; Jagau, T.-C.; Ji, H.; Kaduk, B.; Khistyaev, K.; Kim, J.; Kim, J.; King, R. A.; Klunzinger, P.; Kosenkov, D.; Kowalczyk, T.; Krauter, C. M.; Lao, K. U.; Laurent, A. D.; Lawler, K. V.; Levchenko, S. V.; Lin, C. Y.; Liu, F.; Livshits, E.; Lochan, R. C.; Luenser, A.; Manohar, P.; Manzer, S. F.; Mao, S.-P.; Mardirossian, N.; Marenich, A. V.; Maurer, S. A.; Mayhall, N. J.; Neuscamman, E.; Oana, C. M.; Olivares-Amaya, R.; O'Neill, D. P.; Parkhill, J. A.; Perrine, T. M.; Peverati, R.; Prociuk, A.; Rehn, D. R.; Rosta, E.; Russ, N. J.; Sharada, S. M.; Sharma, S.; Small, D. W.; Sodt, A.; Stein, T.; Stück, D.; Su, Y.-C.; Thom, A. J. W.; Tsuchimochi, T.; Vanovschi, V.; Vogt, L.; Vydrov, O.; Wang, T.; Watson, M. A.; Wenzel, J.; White, A.; Williams, C. F.; Yang, J.; Yeganeh, S.; Yost, S. R.; You, Z.-Q.; Zhang, I. Y.; Zhang, X.; Zhao, Y.; Brooks, B. R.; Chan, G. K. L.; Chipman, D. M.; Cramer, C. J.; Goddard, W. A.; Gordon, M. S.; Hehre, W. J.; Klamt, A.; Schaefer, H. F.; Schmidt, M. W.; Sherrill, C. D.; Truhlar, D. G.; Warshel, A.; Xu, X.; Aspuru-Guzik, A.; Baer, R.; Bell, A. T.; Besley, N. A.; Chai, J.-D.; Dreuw, A.; Dunietz, B. D.; Furlani, T. R.; Gwaltney, S. R.; Hsu, C.-P.; Jung, Y.; Kong, J.; Lambrecht, D. S.; Liang, W.; Ochsenfeld, C.; Rassolov, V. A.; Slipchenko, L. V.; Subotnik, J. E.; Van Voorhis, T.; Herbert, J. M.; Krylov, A. I.; Gill, P. M. W.; Head-Gordon, M. Advances in Molecular Quantum Chemistry Contained in the Q-Chem 4 Program Package. *Mol. Phys.* **2015**, *113*, 184-215.

50. Gutierrez-Baez, R.; Toledo-Antonio, J. A.; Cortes-Jacome, M. A.; Sebastian, P. J.; Vazquez, A. Effects of the SO_4 Groups on the Textural Properties and Local Order Deformation of SnO_2 Rutile Structure. *Langmuir* **2004**, *20*, 4265–4271.

51. Saravanan, K.; Tyagi, B.; Shukla, R. S.; Bajaj, H. C. Solvent Free Synthesis of Methyl Palmitate over Sulfated Zirconia Solid Acid Catalyst. *Fuel* **2016**, *165*, 298–305.

52. Shi, G.; Yu, F.; Wang, Y.; Pan, D.; Wang, H.; Li, R. A Novel One-Pot Synthesis of Tetragonal Sulfated Zirconia Catalyst with High Activity for Biodiesel Production from the Transesterification of Soybean Oil. *Renew. Energy* **2016**, *92*, 22−29.

53. Saravanan, K.; Tyagi, B.; Bajaj, H. C. Nano-Crystalline, Mesoporous Aerogel Sulfated Zirconia as An Efficient Catalyst for Esterification of Stearic Acid with Methanol. *Appl. Catal. B-Environ.* **2016**, *192*, 161–170.

54. Li, F.; Chen, L.; Knowles, G. P.; MacFarlane, D. R.; Zhang, J. Hierarchical Mesoporous SnO_2 Nanosheets on Carbon Cloth: A Robust and Flexible Electrocatalyst for CO_2 Reduction with High Efficiency and Selectivity. *Angew. Chem. Int. Ed.* **2017**, *56*, 505–509; *Angew. Chem.* **2017**, *129*, 520–524.

55. Kim, Y.–H.; Hwang, S.–K.; Kim, J. W.; Lee, Y.–S. Zirconia-Supported Ruthenium Catalyst for Efficient Aerobic Oxidation of Alcohols to Aldehydes. *Ind. Eng. Chem. Res.* **2014**, *53*, 12548−12552.

56. Zhao, X.; Wen, T.; Zhang, J.; Ye, J.; Ma, Z.; Yuan, H.; Ye, X.; Wang, Y. Fe-Doped SnO_2 Catalysts with Both BA and LA Sites: Facile Preparation and Biomass Carbohydrates Conversion to Methyl Lactate MLA. *RSC Adv.* **2017**, *7*, 21678−21685.

57. Sakthivel, R.; Prescott, H. A.; Deutsch, J.; Lieske, H.; Kemnitz, E. Synthesis, Characterization, and Catalytic Activity of $SO_4/Zr_1{-}xSn_xO_2$. *Appl. Catal. A-Gen.* **2003**, *253*, 237–247.

58. Lou, Y.; Ma, J.; Hu, W.; Dai, Q.; Wang, L.; Zhan, W.; Guo, Y.; Cao, X.-M.; Guo, Y.; Hu, P.; Lu, G. Low-Temperature Methane Combustion over Pd/H-ZSM-5: Active Pd Sites with Specific Electronic Properties Modulated by Acidic Sites of H-ZSM-5. *ACS Catal.* **2016**, *6*, 8127−8139.

59. Saad, A. B. M.; Ivanov, V. A.; Lavalley, J. C. Comparative Study of the Effects of Sodium Impurity and Amorphisation on the Lewis Acidity of γ-Alumina. *Appl. Catal. A-Gen.* **1993**, *94*, 71–83.

60. Li, Y.; Zhang, X.–D.; Sun, L.; Zhang, J.; Xu, H.–P. Fatty Acid Methyl Ester Synthesis Catalyzed by Solid Superacid Catalyst SO_4^{2-}/ ZrO_2–TiO_2/La^{3+}. *Appl. Energy* **2010**, *87*, 156–159.

61. Pfaff, F. F.; Kundu, S.; Risch, M.; Pandian, S.; Heims, F.; Pryjomska-Ray, I.; Haack, P.; Metzinger, R.; Bill, E.; Dau, H.; Comba, P.; Ray, K. An Oxocobalt(IV) Complex Stabilized by Lewis Acid Interactions with Scandium(III) Ions. *Angew. Chem. Int. Ed.* **2011**, *50*, 1711–1715; *Angew. Chem.* **2011**, *123*, 1749–1753.

62. Montilla, F.; Morallón, E.; De Battisti, A.; Benedetti, A.; Yamashita, H.; Vázquez, J. L. Preparation and Characterization of Antimony-Doped Tin Dioxide Electrodes. Part 2. XRD and EXAFS Characterization. *J. Phys. Chem. B* **2004**, *108*, 5044−5050.

63. Paunović, V.; Pérez-Ramírez, J. Catalytic Halogenation of Methane: A Dream Reaction with Practical Scope? *Catal. Sci. Technol.* 2019. DOI:10.1039/C9CY00625G

64. Degirmenci, V.; Yilmaz, A.; Uner, D. Selective Methane Bromination over Sulfated Zirconia in SBA-15 Catalysts. *Catal. Today* **2009**, *142*, 30–33.

65. Lee, J.–S.; Kim, S.–Y.; Kwon, S.–J.; Kim, T.–W.; Jeong, S.–Y.; Kim, C.–U.; Lee, K.–Y. Selective Production of p-Xylene from Dimethylfuran and Ethylene over Tungstated Zirconia Catalysts. *J. Nanosci. Nanotechnol.* **2018**, *18*, 1419–1422.

66. Oh, J.; Dash, S.; Lee, H. Selective Conversion of Glycerol to 1,3-Propanediol using Pt-Sulfated Zirconia. *Green Chem.* **2011**, *13*, 2004–2007.

67. Kim, H. J.; Kim, J.–W.; Kim, N.; Kim, T.–W.; Jhung, S. H.; Kim, C.–U. Controlling Size and Acidity of SAPO-34 Catalyst for Efficient Ethylene to Propylene Transformation. *Mol. Catal.* **2017**, *438*, 86–92.

68. Jun, J.–W.; Khan, N. A.; Seo, P. W.; Kim, C.–U.; Kim, H. J.; Jhung, S. H. Conversion of Y into SSZ-13 Zeolites and Ethylene-to-Propylene Reactions over the Obtained SSZ-13 Zeolites. *Chem. Eng. J.* **2016**, *303*, 667–674.

69. Wu, J.–F.; Yu, S.–M.; Wang, W. D.; Fan, Y.–X.; Bai, S.; Zhang, C.–W.; Gao, Q.; Huang, J.; Wang, W. Mechanistic Insight into the Formation of Acetic Acid from the Direct Conversion of Methane and Carbon Dioxide on Zinc-modified H–ZSM-5 Zeolite. *J. Am. Chem. Soc.* **2013**, *135*, 13567–13573.

70. Forester, T. R.; Howe, R. F. In Situ FTIR Studies of Methanol and Dimethyl Ether in ZSM-5. *J. Am. Chem. Soc.* **1987**, *109*, 5076–5082.

71. Priya, S. S.; Bhanuchander, P.; Kumar, V. P.; Dumbre, D. K.; Periasamy, S. R.; Bhargava, S. K.; Kantam, M. L.; Chary, K. V. R. Platinum Supported on H-Mordenite: A Highly Efficient Catalyst for Selective Hydrogenolysis of Glycerol to 1,3-Propanediol. *ACS Sustainable Chem. Eng.* **2016**, *4*, 1212–1222.

72. Choi, S. M.; Seo, M. H.; Kim, H. J.; Kim, W. B. Synthesis and Characterization of Graphene-Supported Metal Nanoparticles by Impregnation Method with Heat Treatment in H_2 Atmosphere. *Synth. Met.* **2011**, *161*, 2405–2411.

73. Ravi, M.; Ranocchiari, M.; van Bokhoven, J. A. The Direct Catalytic Oxidation of Methane to Methanol—A Critical Assessment. *Angew. Chem. Int. Ed.* **2017**, *56*, 16464–16483; Angew. Chem. **2017**, *129*, 16684–16704.

Table 1. Physicochemical Properties of the Three Representative Catalysts Prepared in This Study

catalyst	average crystal size (nm)[a]	sulfur content (wt%)[b]	S_{BET} (m^2 g^{-1})[c]	pore size (nm)[d]	pore volume (cm^3 g^{-1})[d]	acid site distribution (NH_3-mmol g^{-1})[e]			B/L[f]
						weak (< 200 °C)	medium (200-400 °C)	strong (> 400 °C)	
SnO_2	11 (10.1)	-	25	12.7	0.08	0.02	0.14	0.23	-
STO	4 (1.8)	2.6	138	2.4	0.08	2.09	2.34	5.87	2.5
SZ	7 (7.1)	3.0	126	5.1	0.2	1.17	1.61	1.47	7.8

[a] Determined by TEM. The values given in parentheses are estimated from XRD analysis. [b] Analyzed by EDX. [c] Calculated from N_2 sorption data. [d] Calculated using the BJH formalism from the N_2 adsorption (or desorption) branch isotherm. [e] Measured by NH_3-TPD. [f] Brønsted to Lewis acid site ratio determined by pyridine FT-IR technique.

Table 2. Electronic and Structural Parameters by XANES and FT-EXAFS Fitting, respectively, for SnO_2 and STO Catalysts

	XANES parameter		EXAFS parameter				
catalyst	E_0[a] (eV)	WL[b] intensity	interaction	CN[c]	R[d] (Å)	σ^{2}[e] (Å^2)	R factor[f]
SnO_2	29201.6	1.26	Sn-O	6.3±0.7	2.05±0.01	0.0026±0.0007	0.017
			Sn-Sn	1.5±0.9	3.18±0.01	0.0022±0.0023	
			Sn-Sn	5.3±1.6	3.72±0.01	0.0027±0.0012	
STO	29204.6	1.26	Sn-O	6.8±0.5	2.05±0.00	0.0038±0.0006	0.009
			Sn-Sn	0.9±0.4	3.19±0.01	0.0004±0.0016	
			Sn-Sn	4.3±1.1	3.71±0.01	0.0034±0.0010	

[a] Edge energy. [b] White line. [c] Coordination number. [d] Interatomic distance. [e] Debye-Waller factor. [f] Goodness of fit.

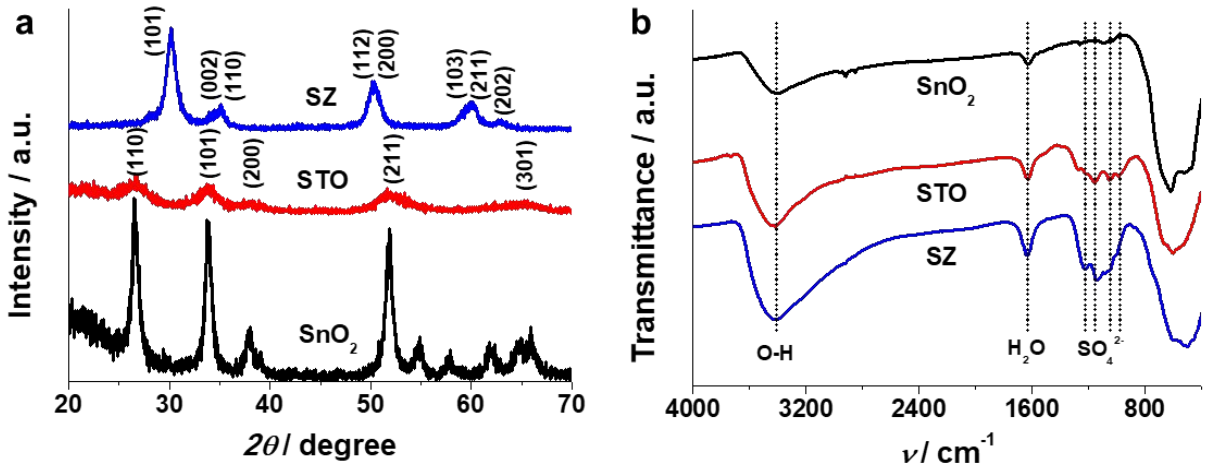

Figure 1. (a) Powder XRD patterns and (b) FT-IR spectra of the three representative catalysts (SnO_2, STO, and SZ) prepared in this study. STO and SZ were sulfated with 3 M H_2SO_4 and calcined at 500 ^oC.

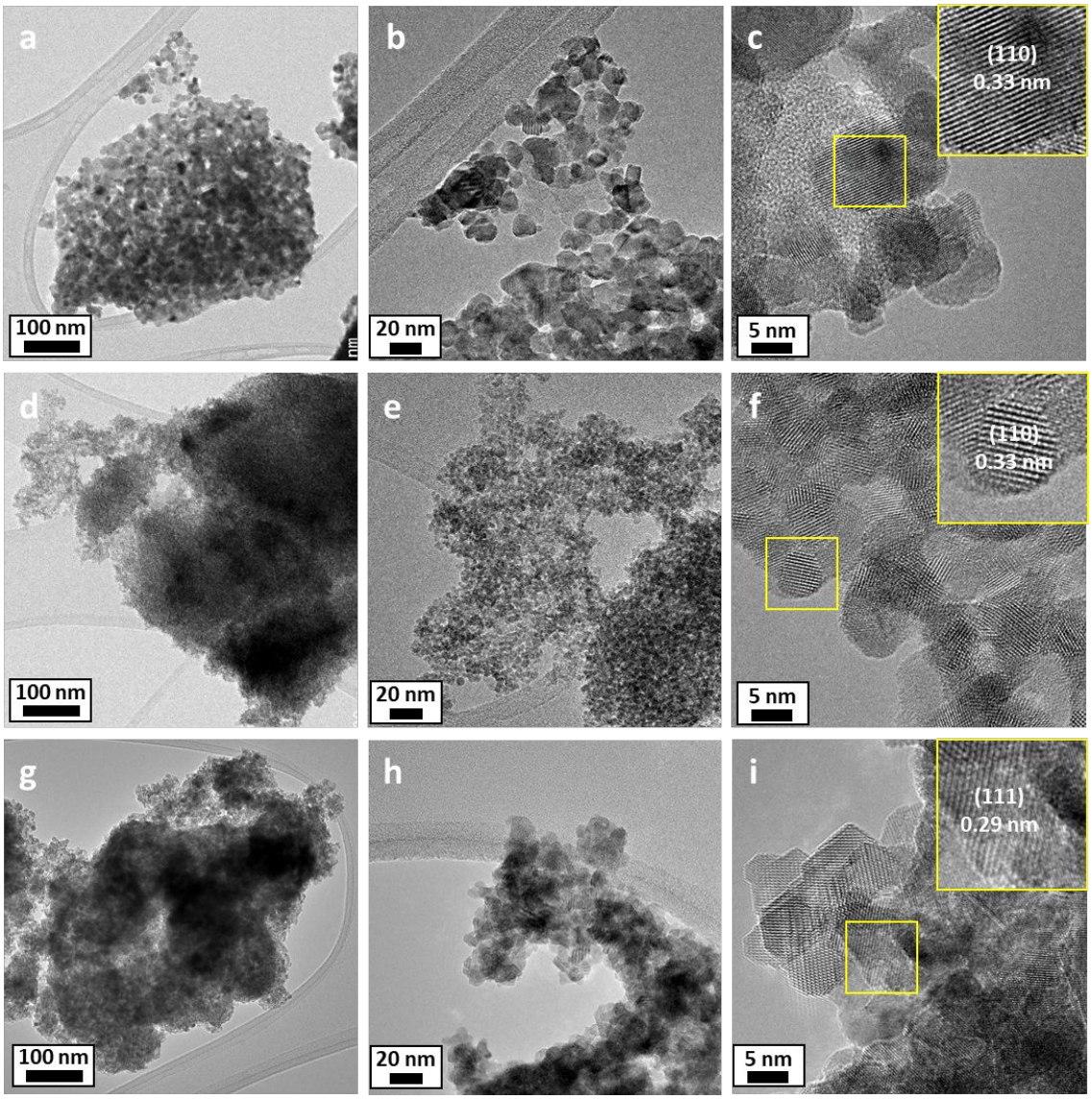

Figure 2. TEM and HRTEM images of the (a-c) SnO_2, (d-f) STO, and (g-i) SZ.

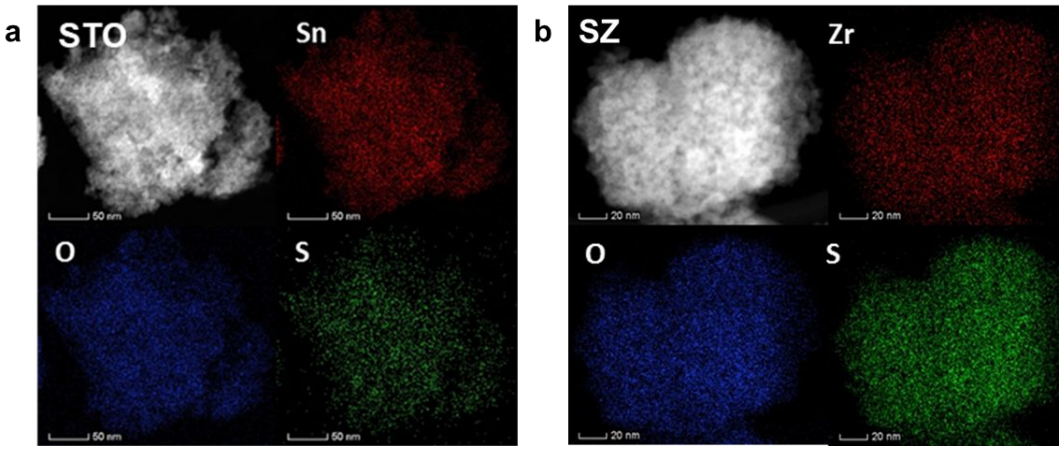

Figure 3. Scanning TEM-EDX elemental mapping images of the (a) STO and (b) SZ catalysts.

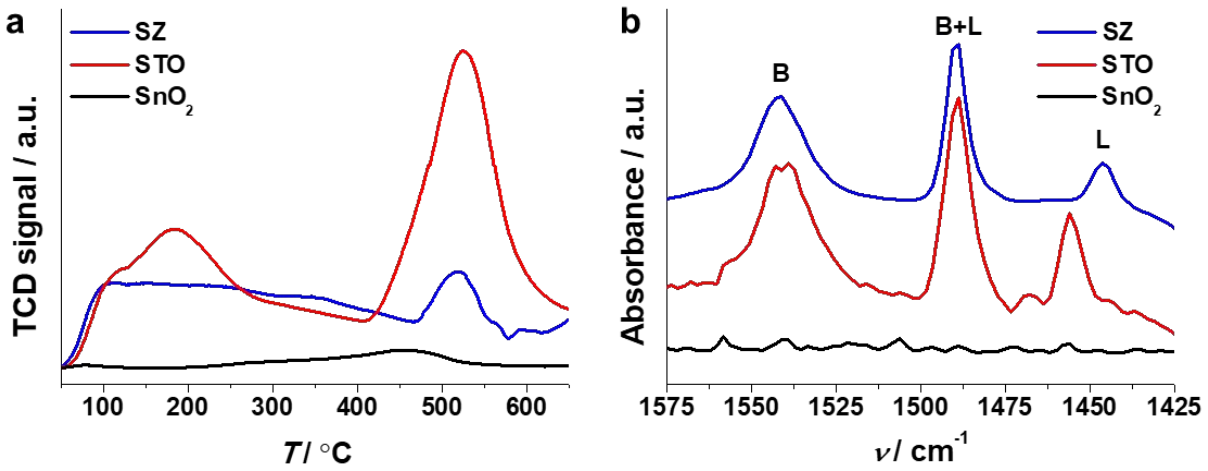

Figure 4. (a) NH_3-TPD profiles and (b) FT-IR spectra of pyridine adsorption over SnO_2, STO and SZ catalysts.

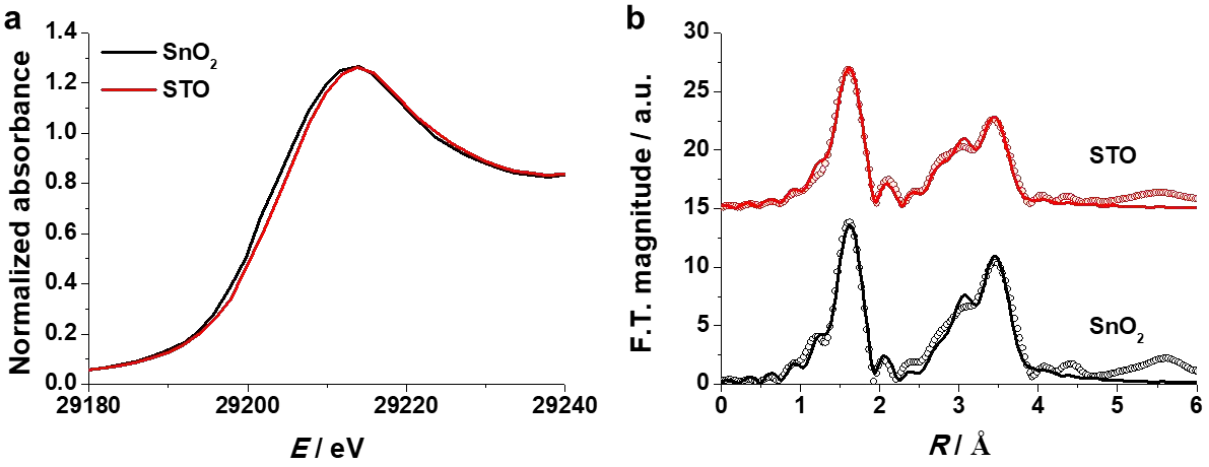

Figure 5. (a) Sn K-edge XANES and (b) FT-EXAFS spectra of the SnO_2 and STO catalysts. (dot: data, line: fit).

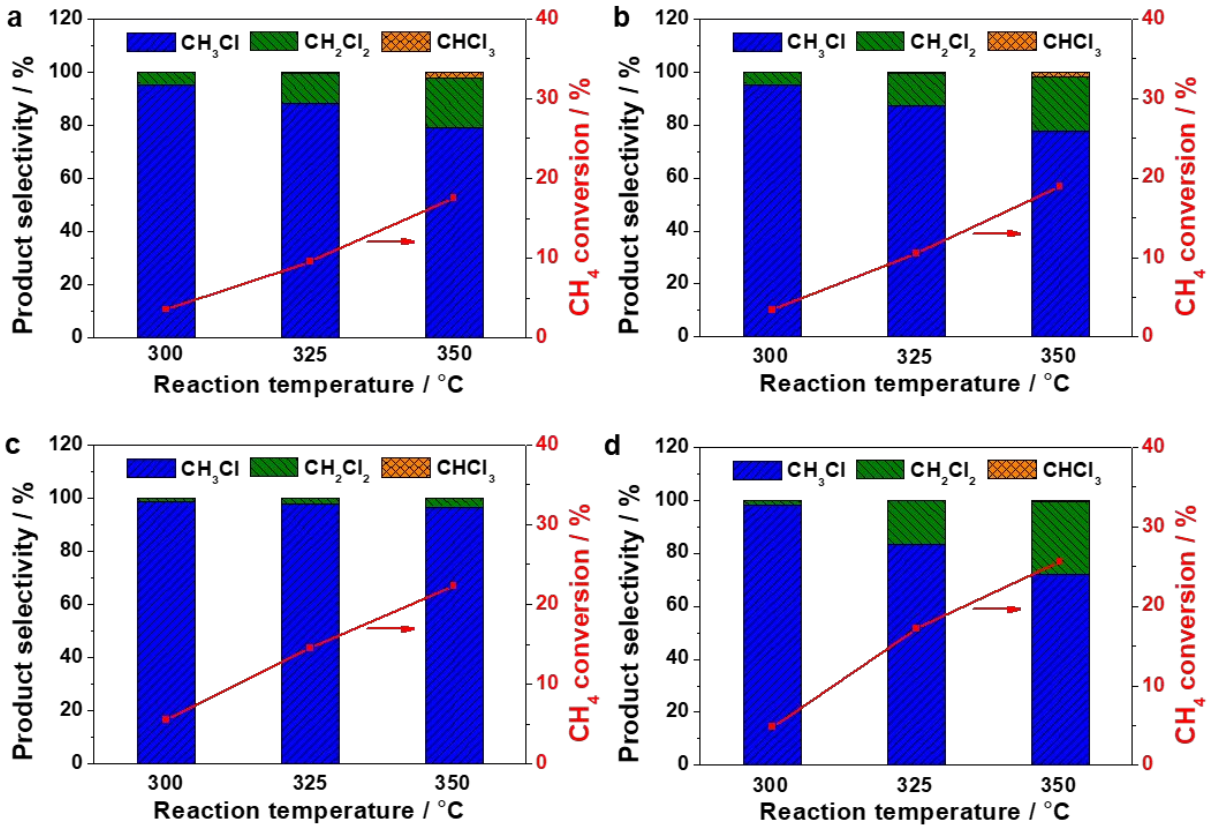

Figure 6. Product selectivity and CH_4 conversion as a function of reaction temperature in CH_4 chlorination over (a) blank, (b) SnO_2, (c) STO, and (d) SZ catalysts (CH_4:Cl_2:He = 1:1:2, 2000 mL h^{-1} g^{-1} GHSV, atmospheric pressure, and 0.5 g of catalyst). Reactions sequentially proceeded with an increasing mode for 2 h at each temperature.

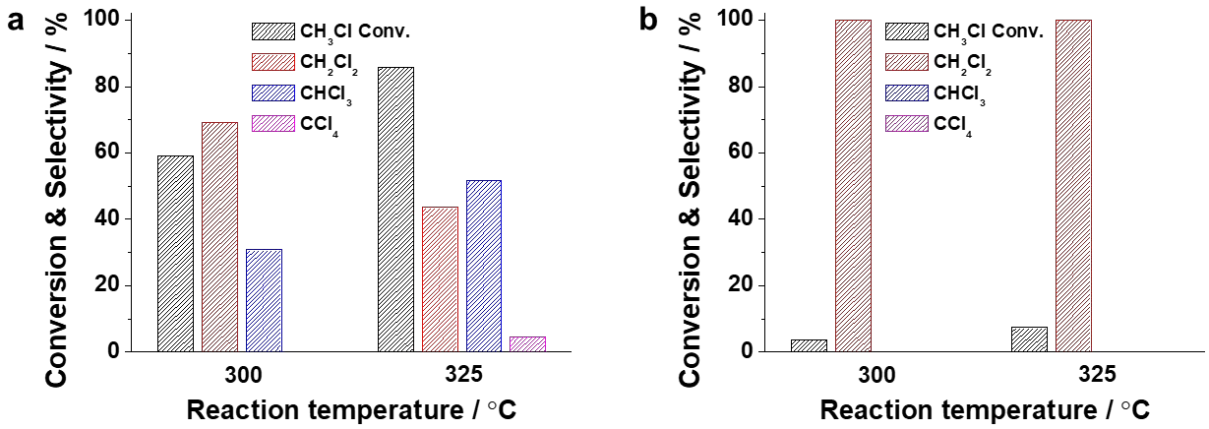

Figure 7. CH_3Cl conversion and product selectivity as a function of reaction temperature in CH_3Cl chlorination over (a) blank and (b) STO catalyst (CH_3Cl:Cl_2:He = 1:2:5, 2000 mL h^{-1} g^{-1} GHSV, atmospheric pressure, and 0.5 g of catalyst).

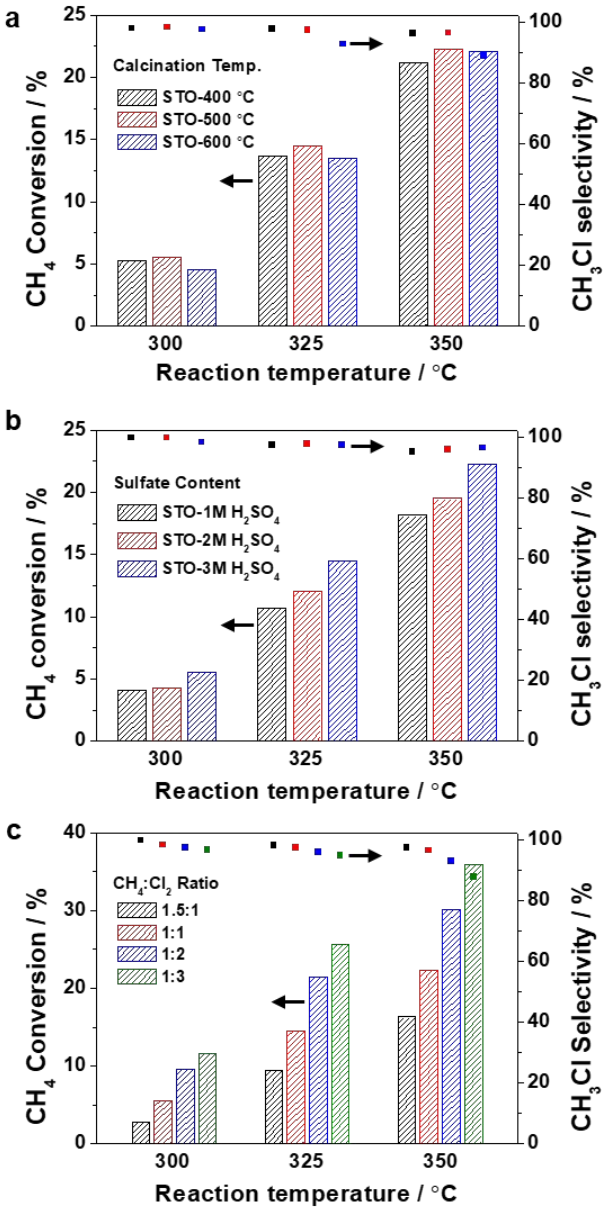

Figure 8. Effects of catalyst preparation and operating conditions on CH_4 chlorination over STO catalysts varying with (a) calcination temperature, (b) sulfate content, and (c) reactant ratio. Reactions sequentially proceeded with an increasing mode for 2 h at each temperature.

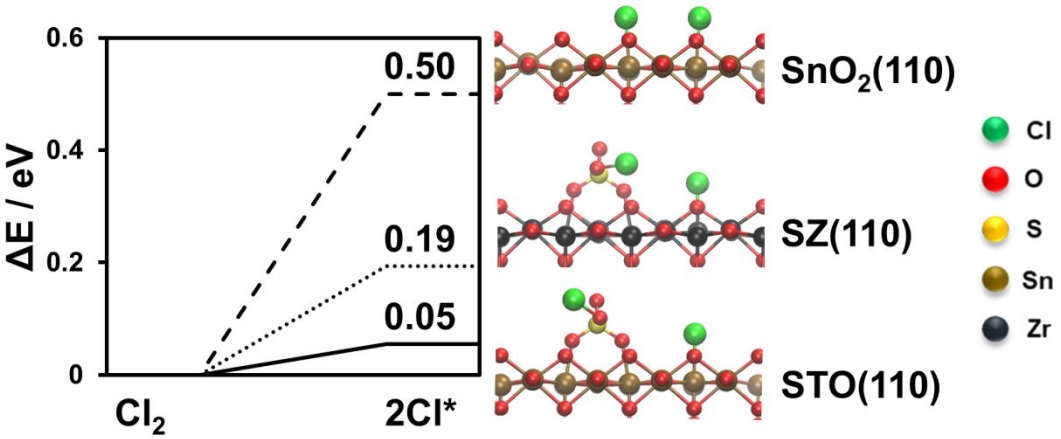

Figure 9. Cl_2 dissociation energies for (110) surfaces of SnO_2 (dashed line), SZ (dotted line), and STO (solid line). For each case, adsorbed Cl atoms were shown together with the exposed surface structure.

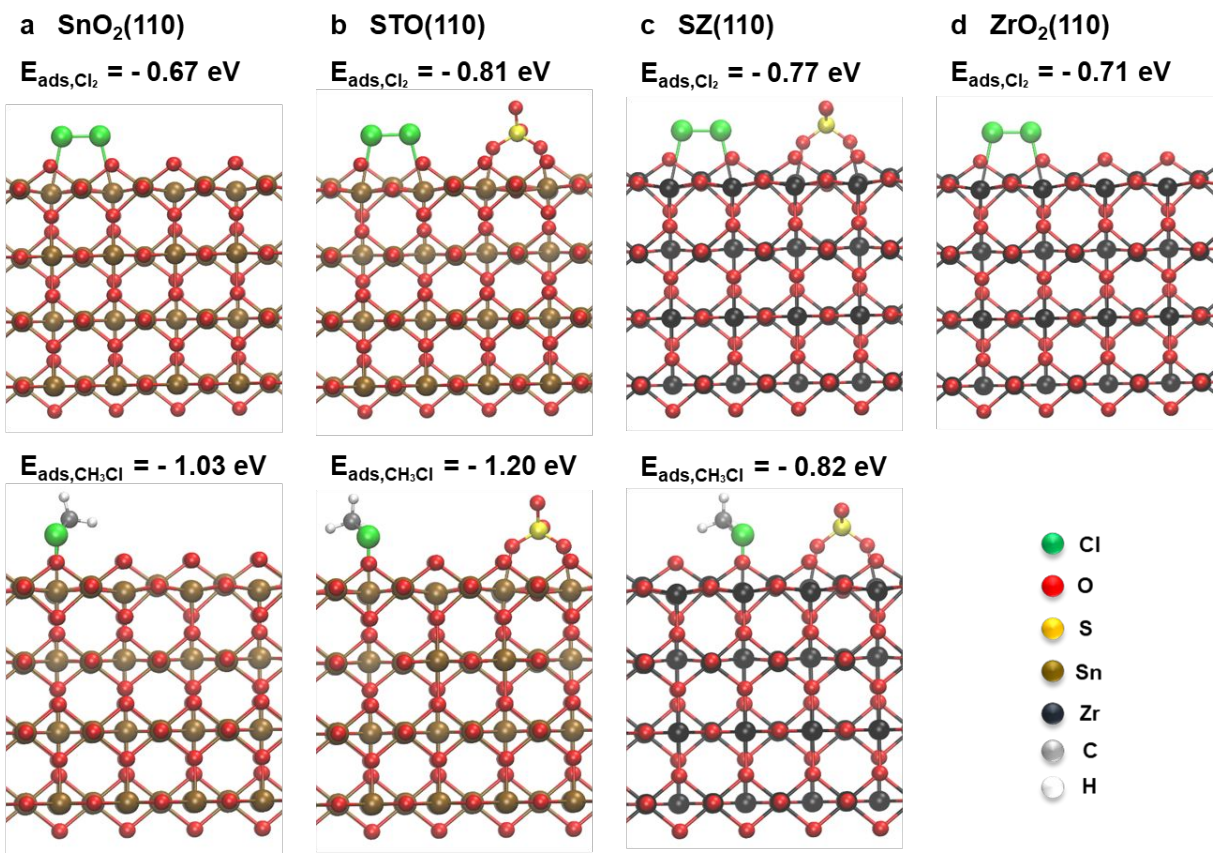

Figure 10. DFT-calculated binding geometries and adsorption energies. Surface structures with adsorbed Cl_2 (top) and CH_3Cl (bottom) molecules on (110) surfaces of (a) SnO_2, (b) STO, (c) SZ, and (d) ZrO_2.

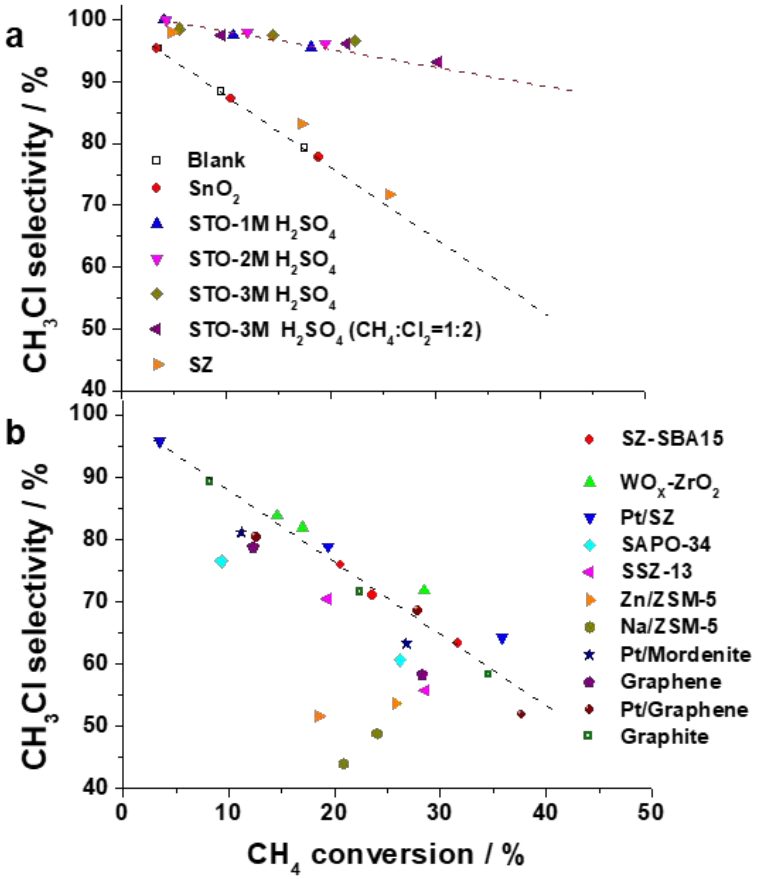

Figure 11. CH_3Cl selectivity as a function of CH_4 conversion over diverse catalysts: (a) this study and (b) reported results. All reference catalysts in this work were prepared according to the literature,[64-72] and tested under the identical reaction conditions (CH_4:Cl_2:He = 1:1:2, 2000 mL h^{-1} g^{-1} GHSV, atmospheric pressure, and 0.5 g of catalyst).

SYNOPSIS TOC

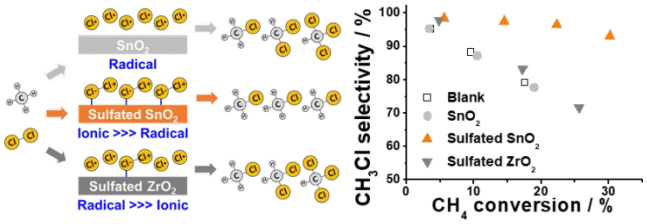

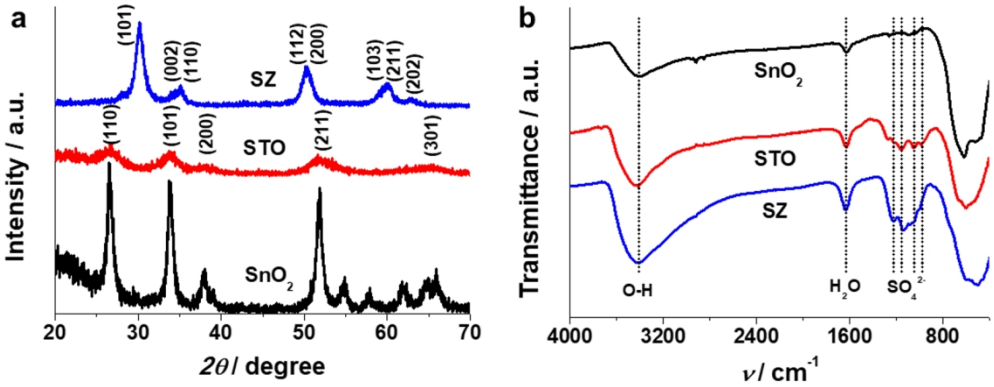

Figure 1. (a) Powder XRD patterns and (b) FT-IR spectra of the three representative catalysts (SnO2, STO, and SZ) prepared in this study. STO and SZ were sulfated with 3 M H2SO4 and calcined at 500 oC.

300x116mm (150 x 150 DPI)

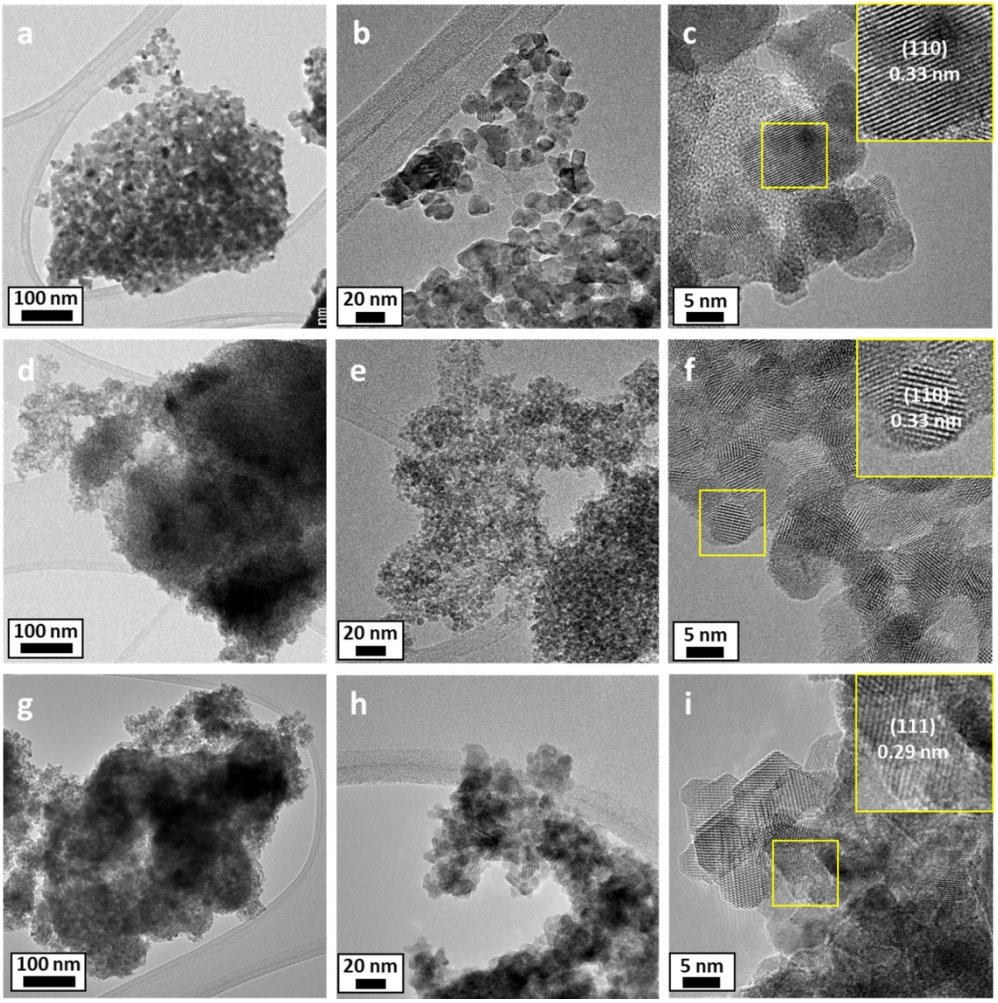

Figure 2. TEM and HRTEM images of the (a-c) SnO2, (d-f) STO, and (g-i) SZ.

300x299mm (150 x 150 DPI)

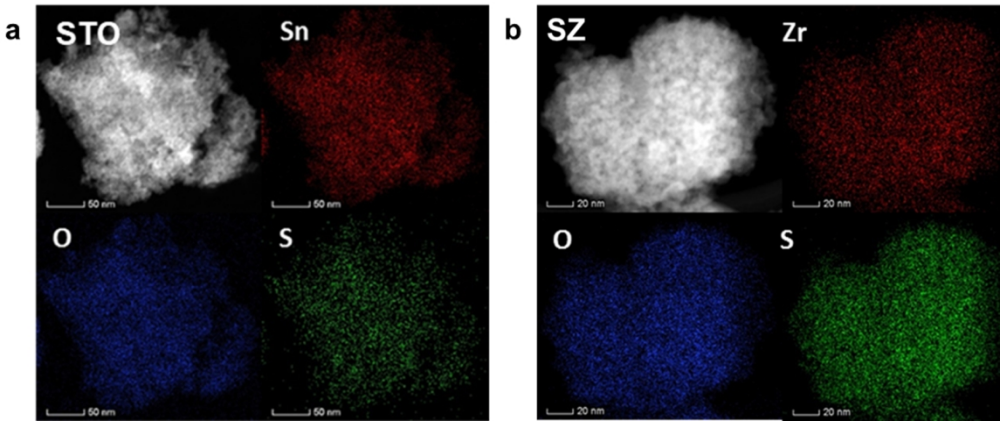

Figure 3. Scanning TEM-EDX elemental mapping images of the (a) STO and (b) SZ catalysts.

300x125mm (150 x 150 DPI)

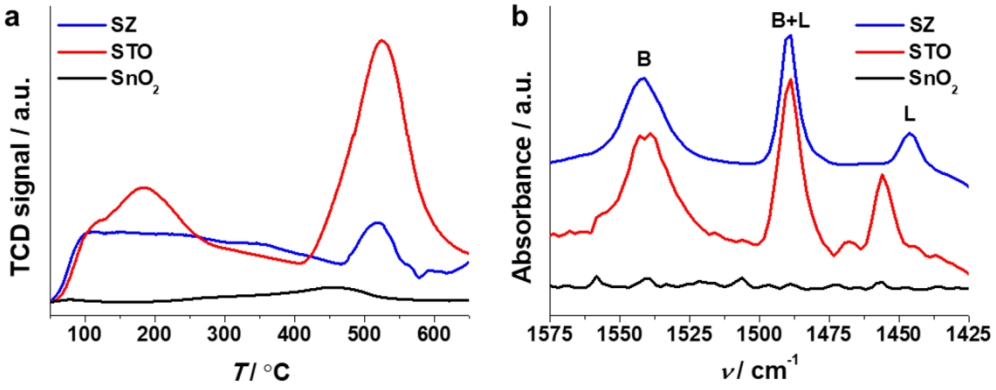

Figure 4. (a) NH3-TPD profiles and (b) FT-IR spectra of pyridine adsorption over SnO2, STO and SZ catalysts.

300x116mm (150 x 150 DPI)

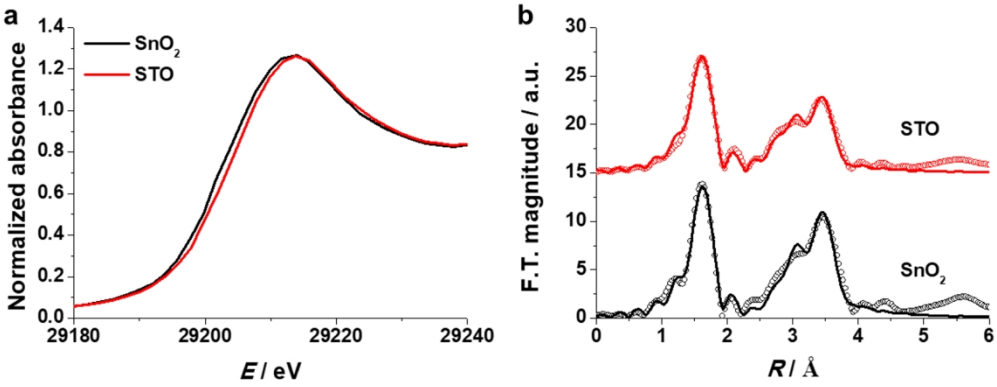

Figure 5. (a) Sn K-edge XANES and (b) FT-EXAFS spectra of the SnO2 and STO catalysts. (dot: data, line: fit).

300x115mm (150 x 150 DPI)

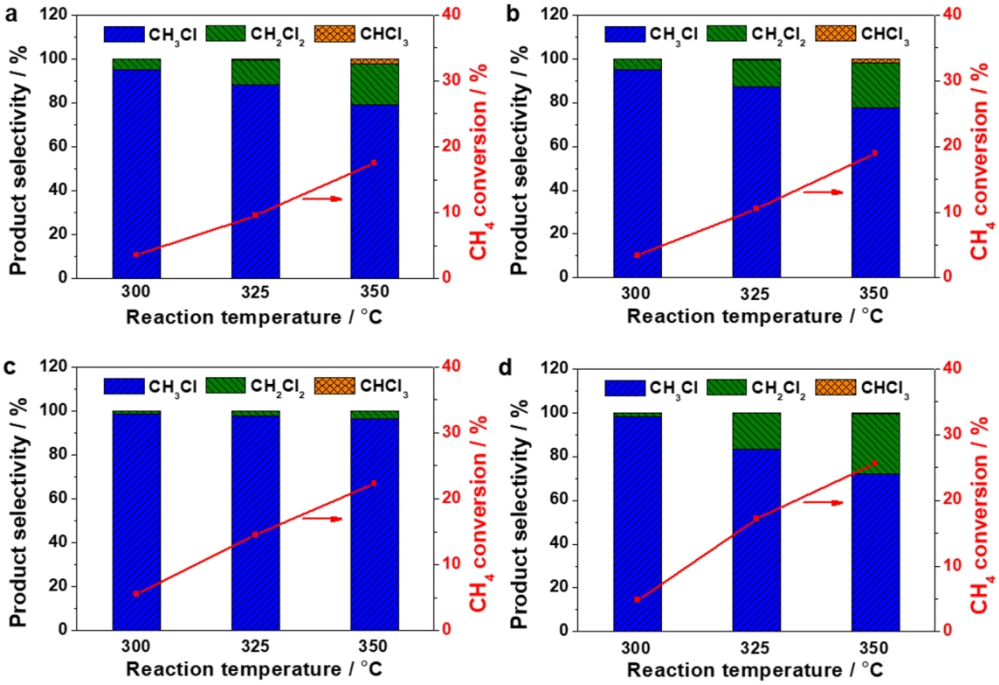

Figure 6. Product selectivity and CH4 conversion as a function of reaction temperature in CH4 chlorination over (a) blank, (b) SnO2, (c) STO, and (d) SZ catalysts (CH4:Cl2:He = 1:1:2, 2000 mL h-1 g-1 GHSV, atmospheric pressure, and 0.5 g of catalyst). Reactions sequentially proceeded with an increasing mode for 2 h at each temperature.

300x207mm (150 x 150 DPI)

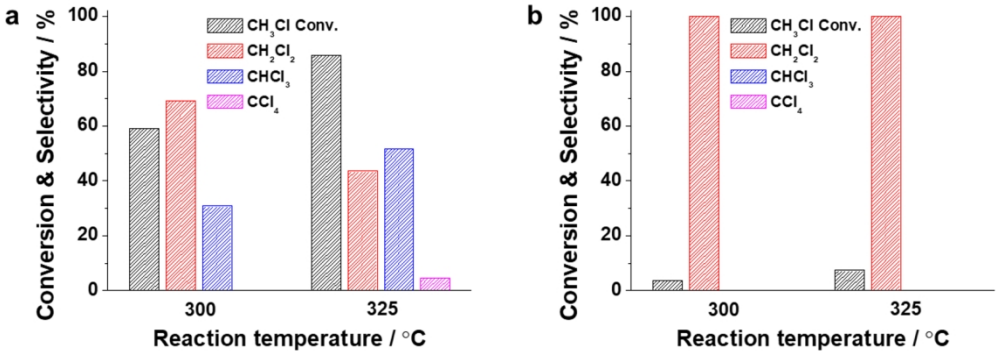

Figure 7. CH3Cl conversion and product selectivity as a function of reaction temperature in CH3Cl chlorination over (a) blank and (b) STO catalyst (CH3Cl:Cl2:He = 1:2:5, 2000 mL h-1 g-1 GHSV, atmospheric pressure, and 0.5 g of catalyst).

300x106mm (150 x 150 DPI)

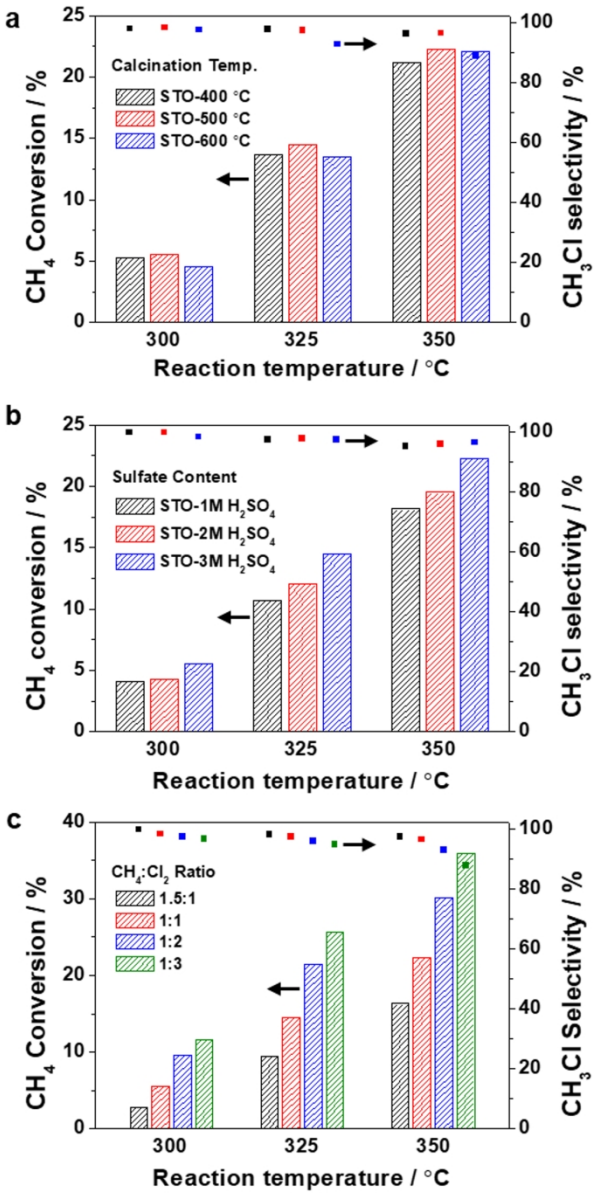

Figure 8. Effects of catalyst preparation and operating conditions on CH4 chlorination over STO catalysts varying with (a) calcination temperature, (b) sulfate content, and (c) reactant ratio. Reactions sequentially proceeded with an increasing mode for 2 h at each temperature.

199x402mm (150 x 150 DPI)

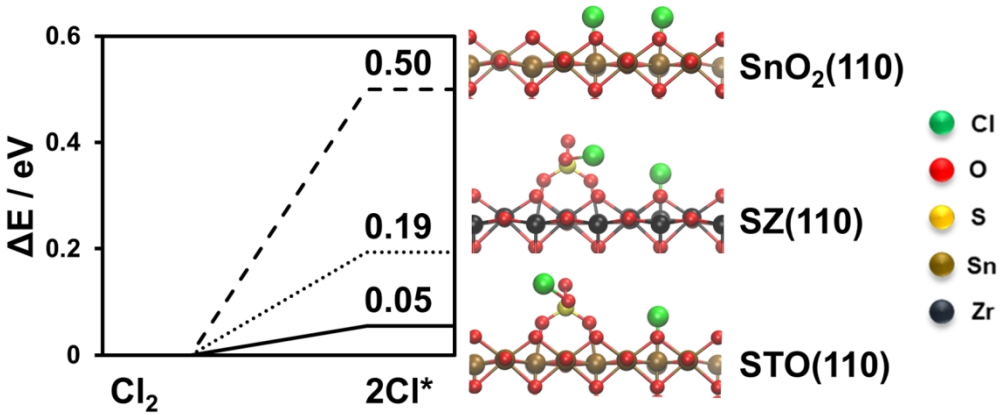

Figure 9. Cl2 dissociation energies for (110) surfaces of SnO2 (dashed line), SZ (dotted line), and STO (solid line). For each case, adsorbed Cl atoms were shown together with the exposed surface structure.

300x125mm (150 x 150 DPI)

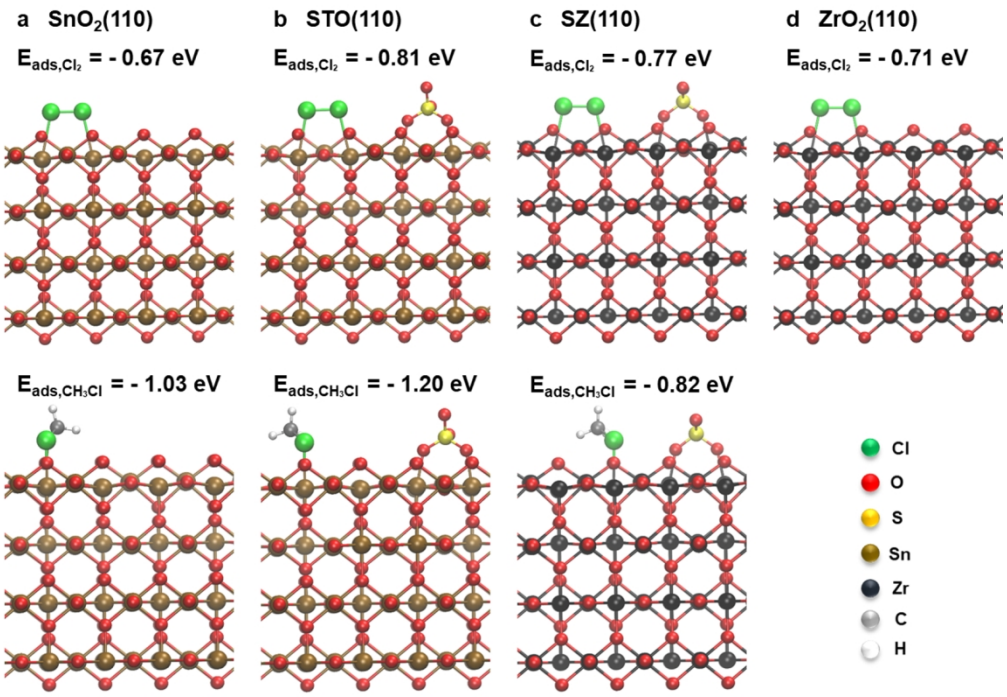

Figure 10. DFT-calculated binding geometries and adsorption energies. Surface structures with adsorbed Cl2 (top) and CH3Cl (bottom) molecules on (110) surfaces of (a) SnO2, (b) STO, (c) SZ, and (d) ZrO2.

300x211mm (150 x 150 DPI)

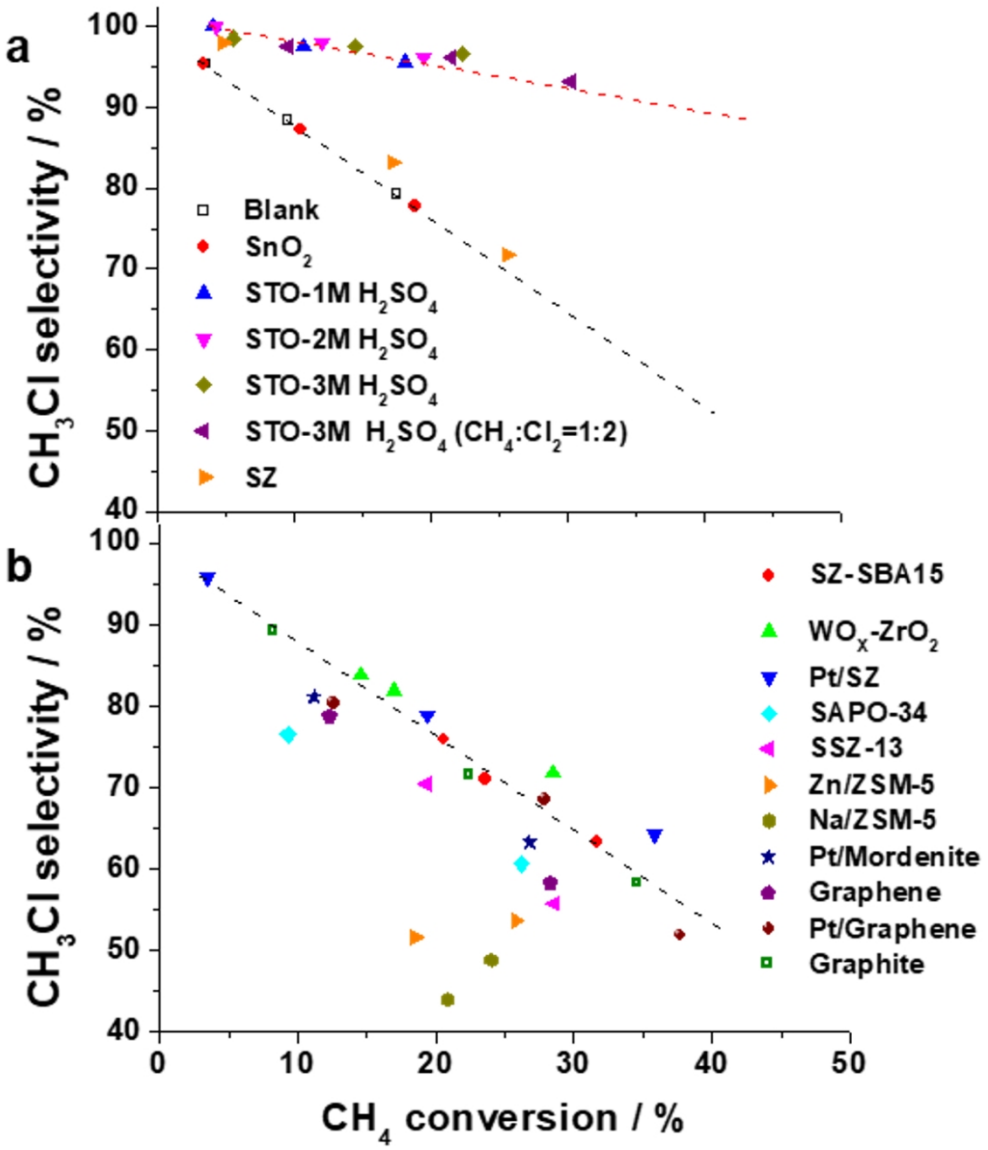

Figure 11. CH3Cl selectivity as a function of CH4 conversion over diverse catalysts: (a) this study and (b) reported results. All reference catalysts in this work were prepared according to the literature, 64-72 and tested under the identical reaction conditions (CH4:Cl2:He = 1:1:2, 2000 mL h-1 g-1 GHSV, atmospheric pressure, and 0.5 g of catalyst).

199x229mm (150 x 150 DPI)

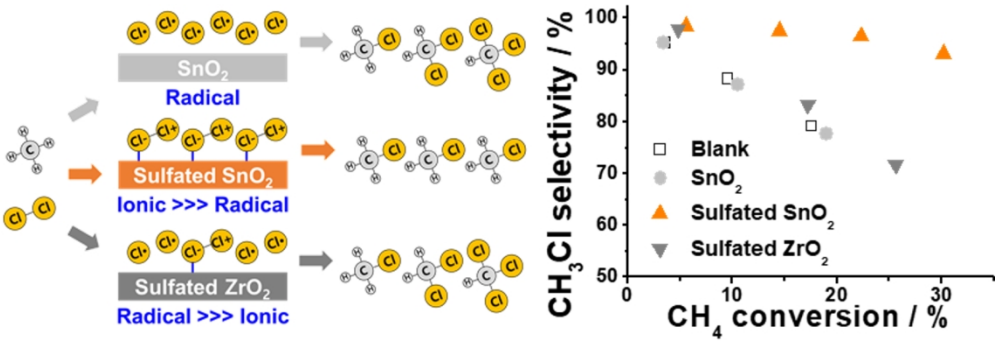

TOC graphic

300x100mm (150 x 150 DPI)

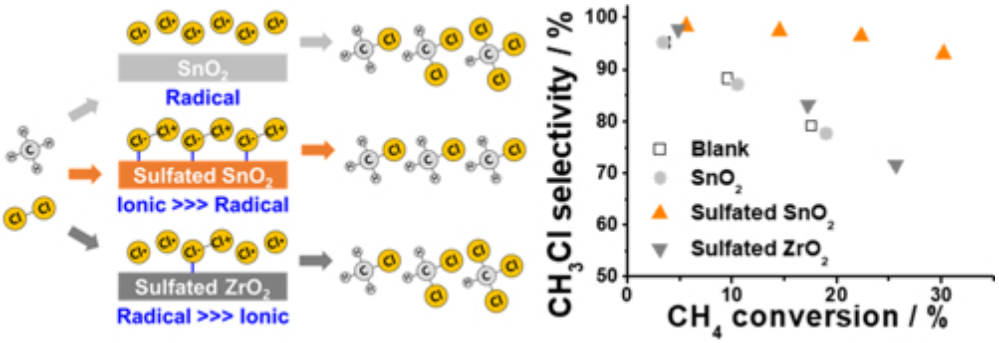

TOC graphic in the actual size

85x28mm (150 x 150 DPI)